To the Graduate Council:

I am submitting herewith a dissertation written by Chieh Wu entitled "Nonlinear Instability of a Baroclinic Flow." I have examined the final copy of this dissertation for form and content and recommend that it be accepted in partial fulfillment of the requirements for the degree of Doctor of Philosophy, with a major in Engineering Science.

Basil N. Antar

Basil N. Antar, Major Professor

We have read this dissertation and recommend its acceptance:

Frank G. Collins

John Steinhoff

Accepted for the Council:

Vice Provost
and Dean of The Graduate School

NONLINEAR INSTABILITY OF A BAROCLINIC FLOW

A Dissertation

Presented for the

Doctor of Philosophy

Degree

The University of Tennessee, Knoxville

Chieh Wu

August 1987

Copyright © Chieh Wu, 1987

All rights reserved

ACKNOWLEDGMENTS

The author should like to record thanks to members of his committee, Drs. Basil N. Antar, Lloyd Crawford, John S. Steinhoff, Trevor H. Moulden and Frank G. Collins, for their assistance in preparing this dissertation. Special gratitude is given to Dr. Basil N. Antar, his major professor, who suggested the nonlinear problem as a dissertation proposal, and who encouraged him to write and develop his own code to find the numerical solutions to this problem.

Sincere thanks are also expressed to The University of Tennessee Space Institute (UTSI) administration for permission to use more computer time in computation and to the UTSI Library personnel for their help in finding a lot of technical literature.

Sincere appreciation is extended to his wife, Susan, for her continuing support and encouragement throughout his study at UTSI with a pile of letters from their Oak Ridge home. Both of them are Christians and thank God for wisdom to complete his study.

The author wishes to especially thank Mrs. Linda W. Hershman for her dependable assistance in typing the final manuscript.

ABSTRACT

The stability for quasi-geostrophic disturbances of atmospheric currents is investigated for a continuously stratified model. The baroclinic disturbances in the atmosphere are initiated as the result of a hydrodynamic instability of the basic zonal current with respect to small perturbations of the flow. The perturbation equation with nonlinear boundary conditions is derived from the nonlinear theory of the quasi-geostrophic potential vorticity, and solved numerically by the pseudospectral method with the aid of the discrete Fourier transform and the fast transform. A numerical computer code is written and developed to obtain wave amplitudes for the spectrally expanded solution which are found from boundary conditions through time integrations by the Adams-Bashforth method.

The optimum time evolution of wave amplitudes depends upon the combination of three factors: grid points, physical plane size, and initial values. After the final time, 14 days, the blow-up in time integrations comes possibly from the instability condition of Eady linear model, atmospheric turbulence, and frontogenesis. Wave patterns show the principal picture of the nonlinear development of a linear wave. At the final time, the initially small perturbations produce a significant disturbance. So contours at the upper level exhibit atmospheric motions similar to cyclone or anti-cyclone, and wave surfaces at three different levels have the thermal wind-shear effect in the perturbed flow.

TABLE OF CONTENTS

LIST OF TABLES

LIST OF FIGURES

FIGURE PAGE

NOMENCLATURE

A	Longitude angle
A_v	Vertical turbulent viscosity coefficient
A(k,l)	Wave amplitudes
B	Latitude angle
B(k,l)	Wave amplitudes
c	Wave phase speed
C_p	Specific heat at constant pressure
D	Characteristic vertical length
DFT	Discrete Fourier transform
E	Ekman number
E_v	Vertical Ekman number
f	Coriolis parameter
F	Froude number
G	Effective gravitational potential
h_B	Elevation of the lower boundary
k	Wave number for x direction
l	Wave number for y direction
L	Characteristic horizontal length
M	Number of grid points in y direction
N	Number of grid points in x direction
P	Pressure
Q	Rate of heat addition per unit mass
r	Radial distance from earth's center
r_0	Earth's radius

Ro_T	Thermal Rossby number
S	Stratification parameter
T_a	Taylor number
U	Characteristic horizontal speed
W	Weighting kernel

Greek Symbols

α	Thermal expansivity
β	Beta-plane
γ	Dissipation parameter
δ	Aspect ratio
Δ	Supercriticality
ε	Rossby number
ζ	Vorticity
θ	Potential temperature
κ	Thermal conductivity
λ	Scalar quantity
ν	Kinematic viscosity
ρ	Fluid density
ϕ	Perturbation stream function
ψ	Stream function
ψ_0	Basic state stream function
ω	Absolute vorticity
Ω	Earth's angular speed

CHAPTER I

INTRODUCTION

Preface

The envelope of air surrounding the earth is the atmosphere with four different regions: troposphere, stratosphere, mesosphere, and thermosphere. The troposphere is of principal interest to most investigations because fronts, jetstreams, cyclones, anti-cyclones, and hurricanes occur in this lowest region.

The motions of the atmosphere are complicated, but the important one is the circulatory motion. Both the earth's rotation and the baroclinicity have profound effects on the circulation and the vorticity in the atmospheric flow. The atmosphere, which is heated by the sun more strongly at the equator than the poles, is a system that is inherently unstable. A simple form of the instability in a stratified fluid occurs when heavier particles lie above lighter particles. The westerly winds in mid-latitudes exhibit large-scale instability. In laboratory experiments, a similar instability is observed in a differentially heated, rotating annulus. The instability which hinges on the noncoincidence of the constant density and the constant pressure surfaces is called baroclinic instability. The essential factors for the baroclinic instability are rotation, stratification, and horizontal temperature gradient.

The baroclinic instability is the most important form of the instability in the large-scale flow of the atmosphere which has the features of being nearly hydrostatic, nearly geostrophic, and wave-like in appearance. The first linear theory of the baroclinic instability in the quasi-geostrophic flow was formulated by Charney [1] and Eady [2]. The development of the finite-amplitude equilibration of the baroclinically unstable flows has been characterized by close interplay between theoretical work, laboratory experiments, and observations of natural geophysical systems. The following review focuses on recent studies in the nonlinear theory and their associated experiments.

Previous Studies

Experimental Studies

The nonlinear baroclinic instability theory was much stimulated by results from laboratory studies of convection in rotating fluids. The most adopted laboratory model is a rotating cylindrical annulus of fluid differentially heated between inner and outer walls as shown in Figure 1. The annulus represents a hemisphere of the earth, the fluid represents the atmosphere, and the motion of the fluid is intended to represent the atmospheric circulation. Much of this laboratory work is discussed by Hide and Mason [3]. The annulus experiments usually exhibit several flow regions as shown in Table 1.

Figure 2 is the typical regime diagram [3] to illustrate the dependence of the mode of convection on the two principal dimensionless parameters: the thermal Rossby number (Ro_T), and the Taylor number (Ta). These numbers are given by

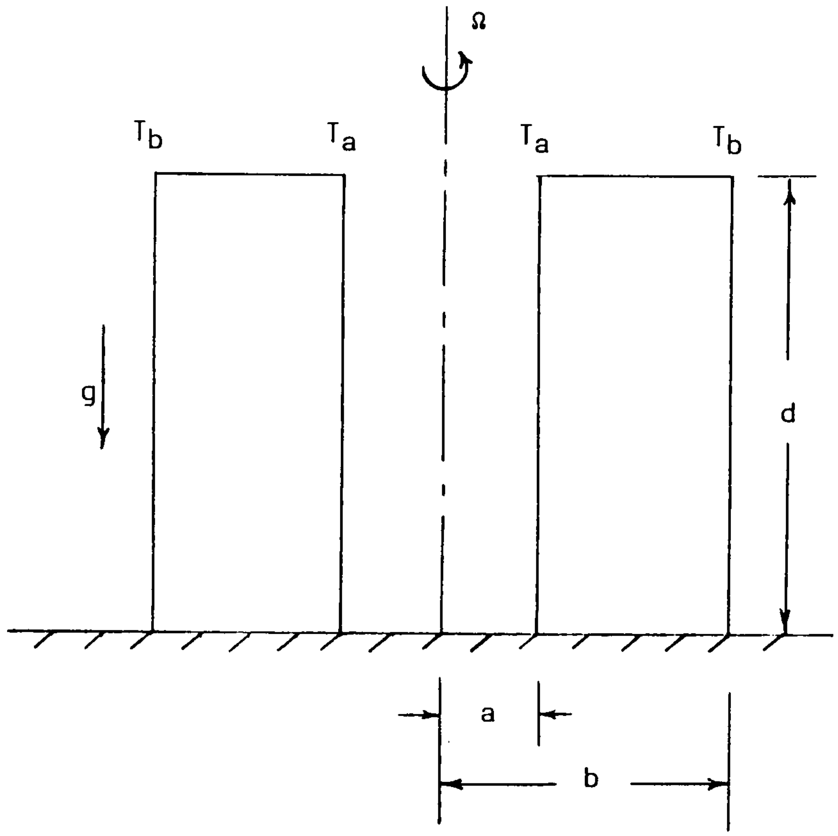

a = inner radius
b = outer radius
d = annulus height
Ω = rotating rate
g = gravitational acceleration
T_a and T_b = respective wall temperatures

Figure 1. Cross-section of a Rotating Fluid Annulus for Baroclinic Instability.

Table 1. Classification of Types of Free Convection in a Rotating Fluid.

Axisymmetric	Nonaxisymmetric
	Regular baroclinic waves Steady waves Vacillation (Wave shape, wave amplitude, wave number, wave dispersion) Irregular baroclinic waves (Geostrophic turbulence)

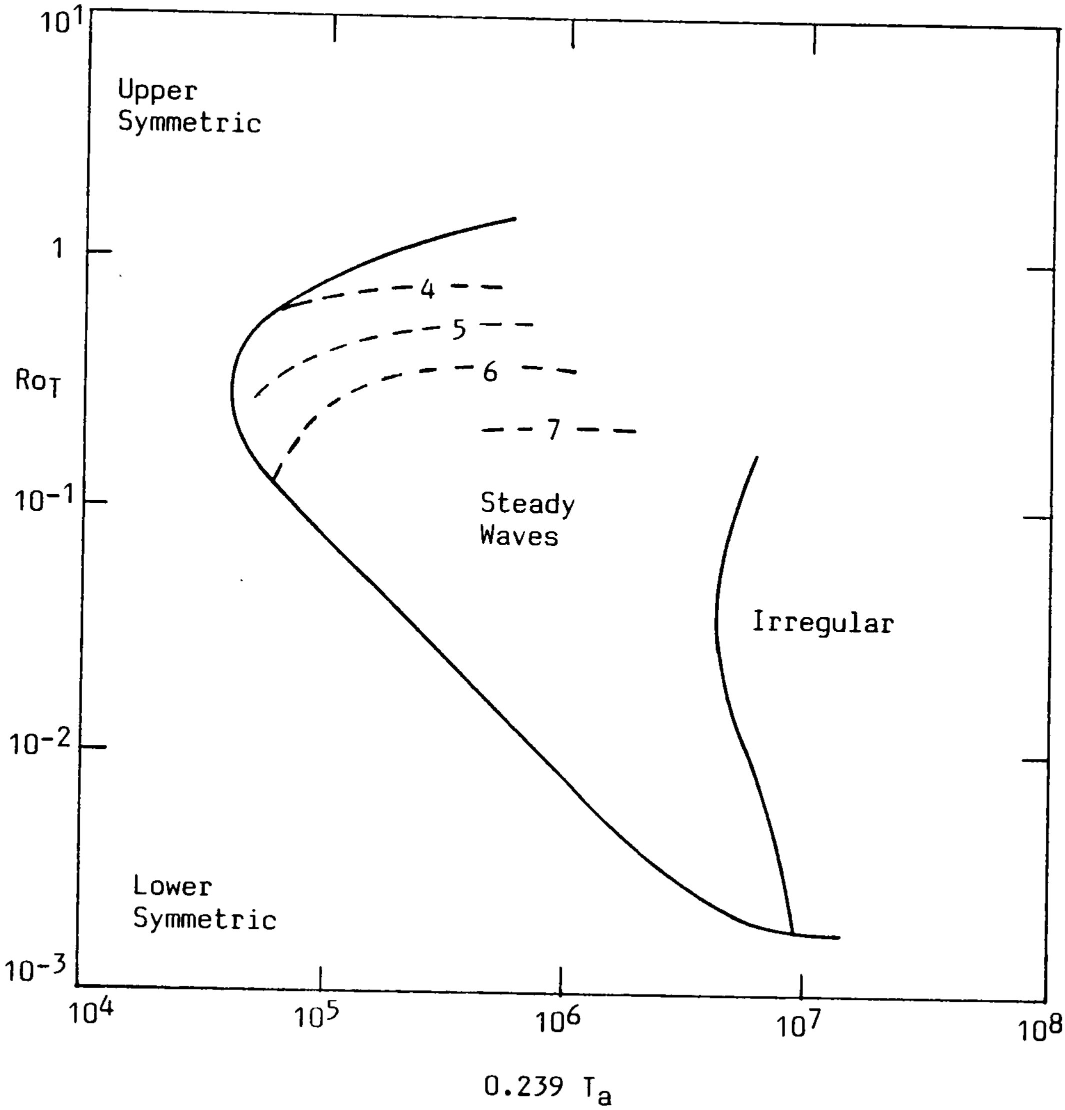

Figure 2. Typical Regime Diagram.

$$Ro_T = \frac{\alpha g d \Delta T}{\Omega^2 (b - a)^2}$$

$$Ta = \frac{4\Omega^2 (b - a)^5}{\nu^2 d} .$$

Where α is the thermal expansivity, ΔT is the temperature difference between outer and inner walls, and ν is the kinematic viscosity. The anvil- or knee-shaped curve in the figure separates the flow into two main parts: axisymmetric regime, and nonaxisymmetric regime. The numbers in the region of steady waves refer to the zonal observed wave number of the dominant wave.

The axisymmetric flow has been divided into two classes according to the circumstances in which it occurs. In the upper symmetric region the axisymmetric flow is stable because of the high static stability set up by the convective motion; whereas, in the lower symmetric region, it is stable because of viscous and conductive dissipation.

Up to now the annulus experiments have not only guided studies concerning the predictability or periodicity of the atmosphere, but also have become the subject of numerous theoretical and numerical studies.

Theoretical Studies

The results of previous theoretical studies of the baroclinic instability in the quasi-geostrophic flow fall into two categories: weakly nonlinear theory, and strongly nonlinear theory. In the first category, the points representing the system under investigation lie within the unstable region and near the marginal curve as in the studies of Pedlosky [4,5,6], Drazin [7,8], Barcilon and Drazin [9], and Chou and Loesch [10,11]. In the second category, general studies with different modes in the unstable region and away from the marginal curve have been conducted by Hoskins [12], Boville [13,14,15], and Weng [16].

Pedlosky [4,5] first used asymptotic methods in a quasi-geostrophic two-layer model to discuss the nonlinear equilibration of baroclinic waves. The results depend on the dissipation parameter γ which is the ratio of the square root of the Ekman number (E) to the Rossby number (ε) of the flow; i.e., $\gamma = \sqrt{E}/\varepsilon$ (E and ε will be defined later in the fourth section of Chapter II). If γ is either equal to zero or much less than one, which corresponds to the inviscid Eady problem, the amplitude of the observed wave should oscillate in time. The steady finite-amplitude waves are obtained for values of γ of the order unity. Pedlosky [6] studied the free-rigid surface configuration in the two-layer model and found that the wave amplitude would have a vacillation which had a growth-decay tendency with the weak dissipation.

Drazin [7,8] also adopted asymptotic methods but in the continuous Eady-type model. The nonlinear extension of Eady's model gave a qualitative description of the interchanges of kinetic and potential energy between the basic flow and large-scale disturbances of the troposphere in mid-latitudes. The slightly unstable basic zonal flows do not develop into turbulence, but into a zonal flow together with a nonlinear wave periodic in space and time. When he included Ekman layers on the rigid top and bottom of the square channel of his model, the results exhibited the baroclinic instability qualitatively similar to that of the two-layer model. The relation between his model and experiments on the differentially heated annulus in the rotating fluid is closer.

Barcilon and Drazin [9] used a weakly nonlinear theory to study the baroclinic instability in the quasi-geostrophic flow of a slightly viscous fluid in a rectangular channel. The basic states differ slightly from Eady's model. Owing to these departures, the critical layers lead to weak instabilities. The weak dissipation is allowed to overcome exactly the growth on a marginal curve different from Eady's. They found that in some regions of parameter space amplitude vacillation occurred.

Chou and Loesch [10,11] used the asymptotic approach, the ad hoc approach, and the spectral numerical approach to study the Eady model modified by Ekman dissipation on the lower boundary and a free upper boundary. The time evolution of the disturbance is generally characterized by a single bump pattern, a growth stage to a maximum amplitude followed by a decay stage. During the decay stage, the spectral solution develops an amplitude vacillation. The asymptotic and the ad hoc solutions qualitatively capture the growth and the decay of the disturbance, but fail to predict vacillation. They also employed both asymptotic and spectral numerical methods to study finite-amplitude dynamics of baroclinic disturbance in the presence of asymmetric Ekman pumping at the lower and upper boundaries. The results exhibit that eventual equilibration, regular vacillation, and chaotic vacillation depend on the actual values of supercriticality, dissipation, stratification parameters, and fundamental zonal wave number.

Hoskins [12] used semi-geostrophic equations in theoretical studies of the baroclinic wave and in a general analysis for the stability of a zonal flow to an infinitesimal perturbation. The perturbation equations are identical with those that would be obtained from the quasi-geostrophic theory. These equations are also used for a numerical and analytical study of the development into the nonlinear regime of the Eady wave instability mode. Both the linear and the nonlinear developments contain many features similar to those observed in atmospheric cyclone disturbances.

Boville [13,14,15] used a two-level quasi-geostrophic model in f-plane and β-plane channels to study strongly nonlinear baroclinic waves undergoing vacillation. The results on f-plane are compared to those of a weakly nonlinear asymptotic theory of amplitude vacillation formulated by Pedlosky [4,5]. Although the two systems give similar results for weak instabilities, they give quite different results for larger instabilities. It is shown that the weakly nonlinear theories do not work well on the β-plane, because nonlinear interactions are not negligible even though only a single wave has any significant amplitude. The mechanism which causes amplitude vacillation has been shown to be substantially different on β-plane than it is on f-plane.

Weng [16] used a modified Eady model to study analytically and numerically the behavior of strongly nonlinear, baroclinic waves in her dissertation. She gave a unified picture that described the four regimes observed in the rotating annulus experiments as shown in Table 1. The transition regions between two regimes are found to be quite narrow except the one between amplitude vacillation and structural vacillation. Her work may help in the basic understanding of transition to more complex regions, like geostrophic turbulence.

Numerical Studies

Quient [17] used the Lorentz model to study properties of the structural vacillation. The Lorentz model is a quasi-geostrophic, two-layer model with a single zonal and two meridional (sin πy and sin $2\pi y$) modes. He simulated five different kinds of vacillation, asymmetric vacillation, and double asymmetric vacillation. All his studies exhibited the structural vacillation without producing the amplitude vacillation.

Quon [18] reproduced almost all of William's results in one-twentieth of the computing time with a mixed spectral and finite difference model; but Williams [19] used the finite difference method to investigate baroclinic annulus waves by means of numerical integration of the three-dimensional, nonlinear Navier-Stokes equations and the heat equation. Quon simplified his studies for interactions in baroclinic flows between mean current and wave, between wave and wave, or between multiple waves because his mixed model permitted the selection of the number of waves and wave numbers.

Klein and Pedlosky [20] used a series of numerical integrations of the two-layer, quasi-geostrophic model to investigate the nonlinear dynamics of baroclinically unstable waves with the Fourier spectral method. Their studies are in some respects similar to Boville's [13, 15], but different from his in the strong supercriticality. The overall behaviors of the solutions are a function of dissipation parameter (γ) and supercriticality (Δ), the difference between the value of the rotational Froude number (F) and its critical value for linear instability (F_c); i.e., $\Delta = F - F_c$. The results are contrasted with results of the weakly nonlinear theory which is valid only at small supercriticality. The aperiodic amplitude waves exist as the supercriticality increases. At much higher supercriticality ($4F_c$), many waves are unstable.

Present Work

Baroclinic flows are ubiquitous in the geophysical fluid dynamics, and they are frequently unstable. Although a great deal of effort has been applied to the development of baroclinically unstable systems as described in the previous section, the present investigation studies the same nonlinear problem with a different approach, and the instability possesses a strong nonlinearity in the three-dimensional case and in the quasi-geostrophic continuous model.

In Chapter II, the problem formulation deals with the derivation of our nonlinear problem from the basis of the geostrophic equations and thermal wind equations to the quasi-geostrophic, potential vortex equations. The linear problem is also presented for the convenience of study. Chapter III pertains to the selection of the numerical method to solve our problems. Of course, a number of baroclinic instability problems were analyzed and solved by the finite difference method or the finite element method, or both. We chose the pseudospectral method based on Fourier series. In Chapter IV, numerical procedures are set up on the theory of discrete Fourier transformation and fast transformation. In Chapter V, the numerical solution is computed in the horizontal plane at lower, middle, and upper levels in the vertical direction. The numerical results are represented and explained with their physical meaning. Chapter VI, the last chapter, gives the conclusion of the present study and the feasibility for further study.

CHAPTER II

PROBLEM FORMULATION

Fundamental Equations

The fundamental equations of atmospheric motions are manifestations of basic laws of physics and thermodynamics. The mathematical relations expressing these laws are given as follows:

a. Continuity equation,

$$\frac{d\rho}{dt} + \rho\nabla\cdot\vec{V} = 0 \tag{2.1}$$

b. Momentum equation,

$$\frac{d\vec{V}}{dt} + 2\vec{\Omega} \times \vec{V} = -\frac{1}{\rho}\nabla P + \nabla G + \vec{F} \tag{2.2}$$

c. Energy equation,

$$\frac{de}{dt} + P\,\frac{d\rho^{-1}}{dt} = \frac{k}{\rho}\nabla^2 T + Q + D \tag{2.3}$$

d. Equation of state,

$$P = \rho RT \tag{2.4}$$

e. Poisson's equation,

$$\theta = T\left(\frac{P_s}{P}\right)^{R/C_p} \tag{2.5}$$

f. Vorticity equation,

$$\frac{d\vec{\omega}}{dt} = \vec{\omega}\nabla\cdot\vec{V} - \vec{\omega}\nabla\cdot\vec{V} + \frac{\nabla\rho \times \nabla P}{\rho^2} + \nabla \times \frac{\vec{F}}{\rho} \tag{2.6}$$

where $\frac{d}{dt} = \frac{\partial}{\partial t} + \vec{V}\cdot\nabla$.

The continuity equation is the general expression of conservation of mass in fluid dynamics. Here ρ is the density and $\vec{V}$ is a velocity vector denoted by (u,v,w) in space.

The momentum equation is written in terms of a rotating coordinate system representing the earth's rotation about its axis with angular velocity $\vec{\Omega} = \Omega\vec{k}$. The term $2\vec{\Omega} \times \vec{V}$ is called the Coriolis force. Here G is the effective gravitational potential, and $\vec{F}$ is the frictional force. If $\vec{F}$ is neglected for large-scale motion and ∇G is replaced by $\vec{g} = g\vec{k}$ only, then Equation (2.2) takes the following form:

$$\frac{d\vec{V}}{dt} = 2\vec{V} \times \vec{\Omega} - \frac{1}{\rho} \nabla P - \vec{g}. \tag{2.7}$$

In the energy equation, e is the internal energy per unit mass, k is the thermal conductivity, Q is the rate of heat addition per unit mass, and D is the dissipative energy.

The equation of state is also called the gas equation. Here R is the gas constant and T is the absolute temperature.

In Poisson's equation, the potential temperature θ is defined as the temperature that a parcel of air at pressure, p, and temperature, T, would attain when its pressure is changed from p to the reference value p_s = 1000 mb by an adiabatic process. Here C_p is the specific heat at constant pressure.

The vorticity equation is obtained from the momentum equation. $\vec{\omega}$ is the absolute vorticity and equal to relative vorticity, $\vec{\omega}_r = \nabla \times \vec{V}$, plus planetary vorticity, $2\vec{\Omega}$. Consider the fluid inviscid, and let λ be any scalar quantity such that $d\lambda/dt = 0$. Taking the scalar product of $\nabla\lambda$ with Equation (2.6) yields

$$\frac{d}{dt}\left(\nabla\lambda\cdot\frac{\vec{\omega}}{\rho}\right) = \nabla\lambda\cdot\frac{\nabla\rho \times \nabla p}{\rho^3}. \tag{2.8}$$

If $\nabla\lambda\cdot(\nabla\rho \times \nabla p) = 0$, i.e., $\lambda = \lambda(\rho,p)$, then

$$\frac{d}{dt}\left(\frac{\vec{\omega}}{\rho}\cdot\nabla\lambda\right) = 0. \tag{2.9}$$

This is called Ertel's theorem. The quantity $\Pi = \vec{\omega}\cdot\nabla\lambda/\rho$ is known as potential vorticity [21].

Baroclinicity of Atmosphere

Generally, the density ρ in a fluid may be expressed by the equation

$$\rho = \rho(p,T) \tag{2.10}$$

where p is pressure and T is absolute temperature. When the relationship (Equation (2.10)) holds, the fluid is said to be baroclinic. Baroclinicity implies that constant pressure surfaces intersect with constant density surfaces. When this relationship becomes $\rho = \rho(p)$, the fluid is said to be barotropic. Barotropicity means that surfaces of constant density (or temperature) are coincident with surfaces of constant pressure. It is the state of zero baroclinicity.

In the atmosphere, the equation of state is expressed in either of the following two ways:

$p = \rho RT$ (for ideal air);

$p = \rho RT\ (1 + 0.6q)$ (for moist air), where q is the specific humidity of the moist air [22]. These two equations indicate that the fluid flow in the atmosphere is generally a baroclinic flow.

Coordinate Systems

The vector momentum equation consists of three scalar component equations in a chosen coordinate system. A natural choice is a spherical coordinate system (A,B,r) with the earth's center of gravity as origin. Here A is the longitude angle, B is the latitude angle, and r is the radial distance from the earth's center as shown in Figure 3. For simplicity we apply a local Cartesian system (x,y,z) with the origin in an arbitrary point, p, in the atmosphere at sea level. The normal convention adopted is that the x-axis points eastwards, the y-axis points northwards, and the z-axis is along the vertical direction, pointing upward. Let $\vec{i},\vec{j},\vec{k}$ denote unit vectors in the x, y, and z directions, respectively. All of them are also shown in Figure 3. The relationship between spherical and local rectangular coordinates is given by

$$x = Ar_0 \cos B_0 \tag{2.11}$$

$$y = (B - B_0)r_0 \tag{2.12}$$

$$z = r - r_0. \tag{2.13}$$

Their derivatives have the following relationships:

$$\partial/\partial A = r_0 \cos B_0 \partial/\partial x \tag{2.14}$$

$$\partial/\partial B = r_0 \partial/\partial y \tag{2.15}$$

$$\partial/\partial r = r - r_0, \tag{2.16}$$

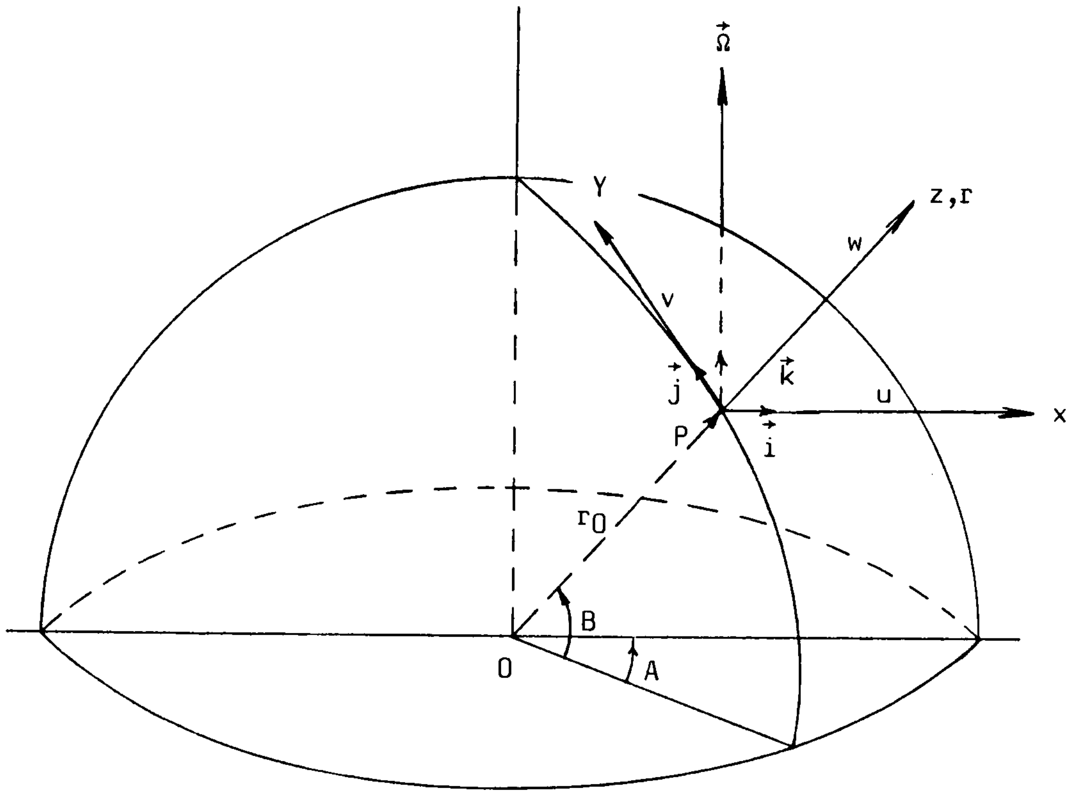

Figure 3. A Local Cartesian Coordinate and Spherical Coordinate System.

where r_0 is earth's radius and B_0 is the central latitude when the point p is at mid-latitudes.

If we denote vectors $\vec{g} = (0,0,-g)$ $\vec{F} = (F_x, F_y, F_z)$, and $\Omega = (0, \Omega \cos B, \Omega \sin B)$, then the component momentum equations in rectangular coordinates are found to be

$$\frac{du}{dt} = -\frac{1}{\rho}\frac{\partial p}{\partial x} + 2\Omega\ (v \sin B - w \cos B) + \frac{F_x}{\rho} \tag{2.17}$$

$$\frac{dv}{dt} = -\frac{1}{\rho}\frac{\partial p}{\partial y} - 2\Omega\ u \sin B + \frac{F_y}{\rho} \tag{2.18}$$

$$\frac{dw}{dt} = -\frac{1}{\rho}\frac{\partial p}{\partial z} + 2\Omega\ u \cos B - g + \frac{F_z}{\rho}\ . \tag{2.19}$$

In spherical coordinates corresponding to the local Cartesian system, the continuity equation becomes

$$\frac{d\rho}{dt} = -\rho\left(\frac{\partial w}{\partial r} + \frac{2w}{r} + \frac{1}{r \cos B}\frac{\partial (v \cos B)}{\partial B} + \frac{1}{r \cos B}\frac{\partial u}{\partial A}\right), \tag{2.20}$$

and the component momentum equations are expressed by

$$\frac{du}{dt} = \frac{uv}{r}\tan B - \frac{uw}{r} + 2\Omega(v \sin B - w \cos B) - \frac{1}{\rho\ r \cos B}\frac{\partial P}{\partial A} + \frac{F_A}{\rho} \tag{2.21}$$

$$\frac{dv}{dt} = -\frac{u^2}{r}\tan B - \frac{vw}{r} - 2\Omega\ u \sin B - \frac{1}{\rho r}\frac{\partial p}{\partial B} + \frac{F_B}{\rho} \tag{2.22}$$

$$\frac{dw}{dt} = \frac{u^2 + v^2}{r} + 2\Omega\ u \cos B - \frac{1}{\rho}\frac{\partial p}{\partial r} - g + \frac{F_r}{\rho}, \tag{2.23}$$

where frictional force $\vec{F} = (F_A, F_B, F_r)$. Since the atmosphere is very shallow compared with r_0, r may be replaced by r_0 when r is undifferentiated.

Scale Analysis

The important motions in the atmosphere are the circulatory motions. Atmospheric circulations are described by sorting out events according to size and time. Small whirlwinds that carry dust skyward are far too small to show up, while cyclones and anti-cyclones reveal large-scale wind patterns. A small eddy, like a dust devil, lasts only a few moments; whereas, a large vortex, like a hurricane, may persist for days. The time and space scales for atmospheric motions are summarized in Table 2 [23] and in Table 3 [24]. These two tables will be helpful in choosing the characteristic length and velocity scales for the numerical computation.

The present study emphasizes the large-scale motion. It does not mean that the motion systems of smaller scales are unimportant, but that the microscale and medium-scale circulations are, to a large extent, controlled by large-scale motion systems. Strong turbulence is formed in regions of large-scale wind fields. Only large-scale motion can be observed and analyzed over a large portion of the globe.

Hereinafter, for convenience in deriving the nondimensional equations, the following scaling has been introduced to relate the dimensional variables (with asterisks) to their dimensionaless counterparts:

$$(x^*, y^*) = L(x, y) \tag{2.24}$$

$$z^* = Dz \tag{2.25}$$

$$(u^*, v^*) = U(u, v) \tag{2.26}$$

$$w^* = \delta U w, \tag{2.27}$$

Table 2. Time and Space Scales for Atmospheric Motions.

Name of Scale	Time Scale	Length Scale	Examples
Macroscale			
Planetary scale	Weeks to years	1,000-40,000 km	Waves in the westerlies
Synoptic scale	Days to weeks	100-5,000 km	Cyclones, anti-cyclones, and hurricanes
Mesoscale	Minutes to days	1-100 km	Land-sea breeze, thunderstorms, and tornadoes
Microscale	Seconds to minutes	Less than 1 km	Turbulence

Table 3. Survey of Atmospheric Motion Systems.

Type of Motion	Horizontal Scale	Vertical Scale	Typical Speed	Lifetime
Large-scale motion:				
Jet stream	10,000 km	5 km	50 m/s	Infinity
Planetary waves	1,000-10,000 km	20-30 km	10-20 m/s	1 week
Tropical cyclones	500-3,000 km	10-15 km	10-30 m/s	1 week
Medium-scale motion:				
Cumulonimbus	10-100 km	5-10 km	1-10 m/s	6 hours
Cumulus	1-5 km	2-4 km	1 m/s	1 hour
Microscale motion:				
Large turbulent eddies	10-100 m	10-100 m	1-10 m/s	100-1,000 s
Small turbulent eddies	1-100 cm	1-100 cm	0.1-1 m/s	10-100 s

where $\delta = D/L$ = aspect ratio

$$r^* = r_0 + z^* = r_0 + Dz \tag{2.28}$$

$$t^* = Lt/U. \tag{2.29}$$

The scaling for pressure, density, and potential temperature is more subtle, but it can be defined [21] as

$$p^* = p_s(z) + \rho_s(z)Uf_0Lp \tag{2.30}$$

$$\rho^* = \rho_s(z)[1 + \varepsilon F\rho] \tag{2.31}$$

$$\theta^* = \theta_s(z)[1 + \varepsilon F\theta] \tag{2.32}$$

where

$f_0 = 2\Omega \sin B_0$ = Coriolis parameter

$\varepsilon = U/(f_0L)$ = Rossby number

$F = f_0^2 L^2/(gD)$ = Froude number

$$p_s = - g\int_0^z \rho_s(z)dz.$$

Here L is a characteristic horizontal length, U is a characteristic horizontal speed, D is a characteristic vertical length or the depth of the fluid, and ρ_s, p_s, and θ_s are functions of z in the basic state, s. Another dimensionless quantity is the Ekman number defined as $E = \nu/(2\Omega L^2)$.

For the large-scale atmospheric motion at mid-latitudes, the ordering relationships are given by

$$\varepsilon = U/(f_0L) \ll 1 \tag{2.33}$$

$$\delta = D/L = O(\varepsilon^2) \tag{2.34}$$

$$L/r_0 = O(\varepsilon) \tag{2.35}$$

$$r^*/r_0 - 1 \leq O(\varepsilon^2) \tag{2.36}$$

$$E < O(\varepsilon). \tag{2.37}$$

Basing upon the ordering, some variables in their related equations may be considered as functions of ε [21] in the following way:

$$(u,v,w) = (u_0,v_0,0) + \varepsilon(u_1,v_1,w_1) + \varepsilon^2(u_2,v_2,w_2) + \cdots \tag{2.38}$$

where $w_0 = 0$ at $z = 0$, and

$$(p,\rho,\theta) = (p_0,\rho_0,\theta_0) + \varepsilon(p_1,\rho_1,\theta_1) + \varepsilon^2(p_2,\rho_2,\theta_2) + \cdots \tag{2.39}$$

Geostrophic Motion

Applying the ordering relationship to the momentum equations, both acceleration and frictional force terms are compared with the Coriolis term. Since their orders are equal to ε or less than ε, respectively, the momentum Equations (2.2) or (2.7) can be simplified as follows:

$$2\Omega\vec{k} \times \vec{V} = -\frac{1}{\rho}\nabla p + g\vec{k}. \tag{2.40}$$

It means that the Coriolis force is balanced by the horizontal pressure force.

Similary in Equation (2.17), the vertical velocity, w, is small of order ε^2 and can be neglected. In Equation (2.19), the order of term $2\Omega u \cos B$ is smaller than that of g and can also be neglected. Therefore, Equations (2.17) through (2.19) are simplified in the following way:

$$fv = \frac{1}{\rho}\frac{\partial p}{\partial x} \tag{2.41}$$

$$fu = -\frac{1}{\rho}\frac{\partial p}{\partial y} \tag{2.42}$$

$$0 = -\frac{1}{\rho}\frac{\partial p}{\partial z} - g, \tag{2.43}$$

where f is the Coriolis parameter; positive in the northern hemisphere, negative in the southern hemisphere, zero at the equator, and equal to $10^{-4}s^{-1}$ at 43.3° latitude angle. Equation (2.43) is the hydrostatic approximation in the vertical direction. Equations (2.41) and (2.42) are geostrophic approximations and can be combined into the following form in the horizontal plane (subscript with H) and shown in Figure 4:

$$f\vec{k} \times \vec{V}_H = - \nabla_H P/\rho$$

where $\vec{V}_H = (u,v)$ and $\nabla_H = (\partial/\partial x + \partial/\partial y)$.

Under the condition of the geostrophic approximations, the large-scale atmospheric motion is called the geostrophic motion. The wind with velocity of geostrophic motion is called geostrophic wind. The vertical variation of geostrophic wind is the thermal wind. By the geostrophic and hydrostatic approximation with the aid of the gas equation, the thermal wind equations [25] are presented by

$$\frac{\partial u}{\partial z} = -\frac{g}{fT}\frac{\partial T}{\partial y} + \frac{u}{T}\frac{\partial T}{\partial z} \tag{2.44}$$

$$\frac{\partial v}{\partial z} = \frac{g}{fT}\frac{\partial T}{\partial x} + \frac{v}{T}\frac{\partial T}{\partial z}. \tag{2.45}$$

In a barotropic atmosphere there can be no increase of geostrophic wind with height because of $\partial u/\partial z = \partial v/\partial z = 0$. However, in a baroclinic atmosphere, we can show that the vertical wind shear depends mainly upon the horiztonal temperature gradients.

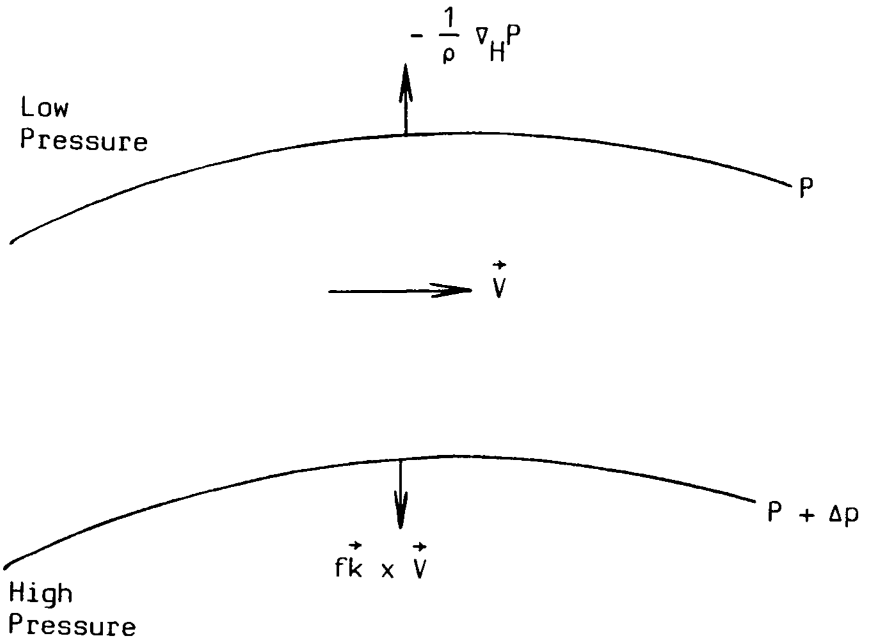

Figure 4. Geostrophic Approximation.

By the definition of the geopotential Φ,

$$d\Phi = g dz = - dp/\rho, \tag{2.46}$$

the geostrophic wind equations in isobaric coordinates [26] are expressed by

$$fu = - \left(\frac{\partial \Phi}{\partial y}\right)_p \tag{2.47}$$

$$fv = \left(\frac{\partial \Phi}{\partial x}\right)_p . \tag{2.48}$$

Differentiating Equations (2.47) and (2.48) with respect to p and using Equations (2.43) and (2.46), we get the following results for a perfect gas

$$\frac{\partial u}{\partial z} = - \frac{g}{fT} \left(\frac{\partial T}{\partial y}\right)_p \tag{2.49}$$

$$\frac{\partial v}{\partial z} = \frac{g}{fT} \left(\frac{\partial T}{\partial x}\right)_p . \tag{2.50}$$

Their vector form is

$$\frac{\partial \vec{V}_H}{\partial z} = \frac{g}{fT} \vec{k} \times (\nabla T)_p . \tag{2.51}$$

Thus the increase of the horizontal velocity with height depends upon the horizontal gradient of the temperature within the surfaces of constant pressure.

Quasi-geostrophic Potential Vorticity Equation

The quasi-geostrophic motion is a particular class of motions, i.e., the large-scale, essentially geostrophic motion. In a shallow, rotating layer of homogeneous and stratified fluid, applying the scaling and ordering relationships to the continuity and momentum

Equations (2.20) and (2.23), the conserved equation in the quasi-geostrophic motion can be obtained by

$$\frac{d}{dt}\left[\zeta_0 + \beta y + \frac{1}{\rho_s}\frac{\partial}{\partial z}\left(\frac{\rho_s\theta_0}{S}\right)\right] = 0, \tag{2.52}$$

where $d/dt = \partial/\partial t + u_0\partial/\partial x + v_0\partial/\partial y$.

To the lowest order fluid field, the geostrophic equations are presented by

$$u_0 = -\partial p_0/\partial y \tag{2.53}$$

$$v_0 = \partial p_0/\partial x \tag{2.54}$$

$$\rho_0 = -(1/\rho_s)\,\partial\,(\rho_s p_0)/\partial z, \tag{2.55}$$

and the potential temperature equation is expressed by

$$\theta_0 = \partial p_0/\partial z. \tag{2.56}$$

Thus, the thermal wind equations are given by

$$\frac{\partial}{\partial z}(\vec{V}_0) = \vec{k} \times \nabla\theta_0, \tag{2.57}$$

and the vorticity equation is denoted by

$$\zeta_0 = \frac{\partial V_0}{\partial x} - \frac{\partial U_0}{\partial y}. \tag{2.58}$$

Concerning β, the beta-plane is deinfed as a plane where the Coriolis parameter, f, is approximated by $f = f_0 + \beta y$ where $\beta = df/dy$ is assumed to be constant in the present case.

S is called the stratification parameter, as the fluid is stratified by a heavier fluid underlying a lighter one. It is defined as

$$S = \frac{N^2 D^2}{f_0^2 L^2},$$

where N is the Brunt-väisälä frequency. This frequency is also called the buoyancy frequency [26]. It is defined as

$$N^2 = \frac{g}{\theta}\frac{d\theta}{dz},$$

and is a measure of the static stability of the environment [27].

Note that Equations (2.53) and (2.54) show that p_0 possesses, in this case, the same definition as the stream function in two-dimensional plane flow, i.e., $\psi = p_0$, and Equation (2.52) becomes

$$\left(\frac{\partial}{\partial t} + \frac{\partial\psi}{\partial x}\frac{\partial}{\partial y} - \frac{\partial\psi}{\partial y}\frac{\partial}{\partial x}\right)\left[\nabla_H^2 \psi + \frac{1}{\rho_s}\frac{\partial}{\partial z}\left(\frac{\rho_s}{S}\frac{\partial\psi}{\partial z}\right) + \beta y\right] = 0. \qquad (2.59)$$

This is the quasi-geostrophic potential vorticity equation and is very important in our study.

The boundary conditions to Equation (2.59) are determined by vertical velocity, vorticity, bottom topography, and upper-surface status.

The lower-boundary condition depends on the Ekman layer [21] and is presented by

$$w_1(x,y,0) = \frac{E_v^{\frac{1}{2}}}{2\varepsilon}\zeta_0(x,y) + \vec{V}_0 \cdot \nabla\left(\frac{h_B}{\varepsilon D}\right). \qquad (2.60)$$

Here E_v is the vertical Ekman number defined as $2A_v/(fD^2)$ where A_v is called the vertical turbulent viscosity coefficient [21], and $h_B(x,y)$ is the elevation of the lower boundary above the reference level $z = 0$, as shown in Figure 5.

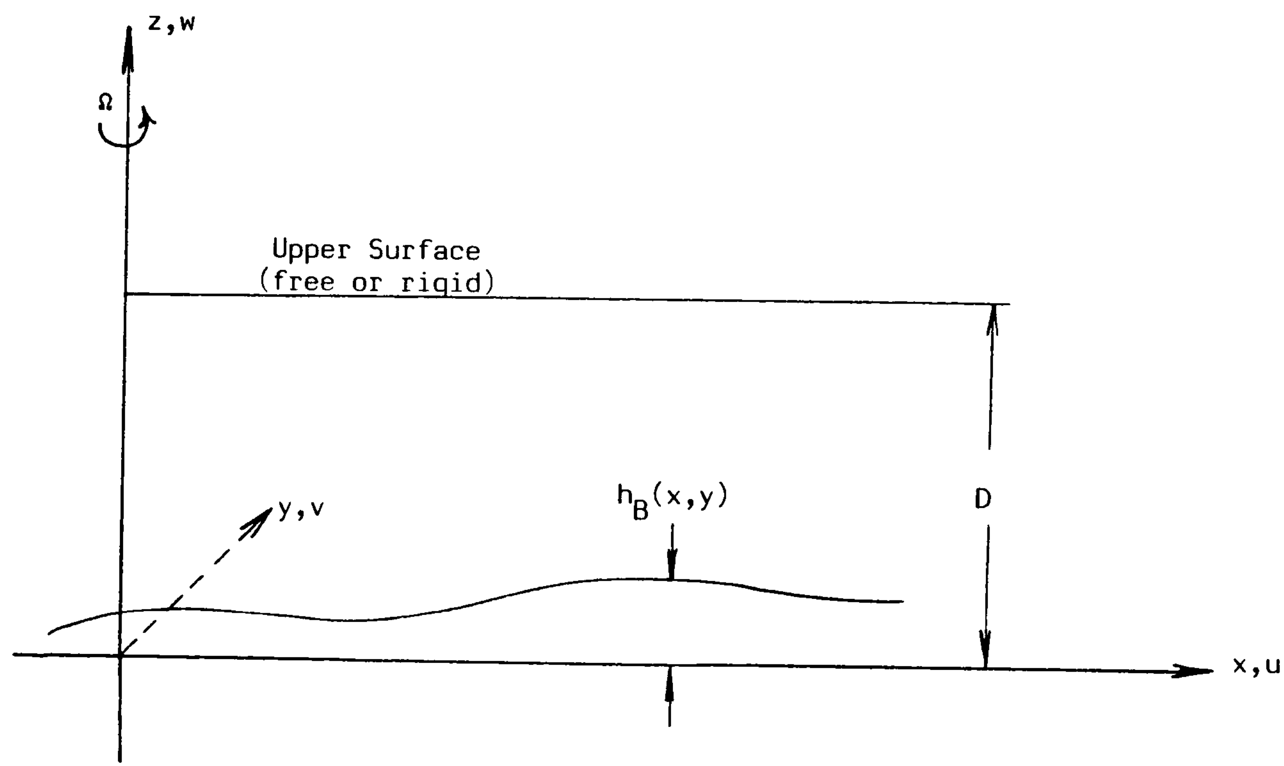

Figure 5. Boundary Conditions.

In quasi-geostrophic scaling and ordering, we have

$$\frac{h_B}{D} = \epsilon\eta_B(x,y) \tag{2.61}$$

$$w_1 = -\frac{1}{S}\frac{d\theta_0}{dt}. \tag{2.62}$$

Substituting Equations (2.61) and (2.62) into (2.60) yields

$$\frac{1}{S}\left(\frac{d\theta_0}{dt}\right)_{z=0} = -\frac{E_v^{\frac{1}{2}}}{2\epsilon}\zeta_0(x,y) - \vec{V}_0\cdot\nabla\eta_B(x,y). \tag{2.63}$$

The upper-boundary condition is given by

$$w_1(x,y,1) = \frac{E_v^{\frac{1}{2}}}{2\epsilon}\left[\zeta_T(x,y) - \zeta_0(x,y)\right] \tag{2.64}$$

where ζ_T is upper vorticity at the level $z = 1$. If the fluid flow is bounded above by a free or rigid horizontal surface, then Equation (2.64) is expressed in the following two boundary conditions:

$$\frac{1}{S}\frac{d\theta_0}{dt} = 0 \qquad \text{(free)} \quad \text{at } z = 1 \tag{2.65}$$

$$\frac{1}{S}\frac{d\theta_0}{dt} = \frac{E_v^{\frac{1}{2}}}{2\epsilon}\zeta_0(x,y) \quad \text{(rigid)} \quad \text{at } z = 1. \tag{2.66}$$

Substituting Equations (2.53), (2.54), (2.56), and (2.58) into (2.63), (2.65), and (2.66) with the aid $\psi = p_0$, the equation for the lower boundary becomes

$$\frac{d}{dt}\left(\frac{\partial\psi}{\partial z}\right) + S\left(\frac{\partial\psi}{\partial x}\frac{\partial\eta_B}{\partial y} - \frac{\partial\psi}{\partial y}\frac{\partial\eta_B}{\partial x}\right) = -\frac{SE_v^{\frac{1}{2}}}{2\epsilon}\nabla^2\psi \tag{2.67}$$

while the equations for the upper boundary are

$$\frac{d}{dt}\left(\frac{\partial\psi}{\partial z}\right) = 0 \qquad \text{(free)} \tag{2.68}$$

$$\frac{d}{dt}\left(\frac{\partial\psi}{\partial z}\right) = \frac{SE_v^{\frac{1}{2}}}{2\epsilon}\ \nabla^2\psi \quad \text{(rigid)} \tag{2.69}$$

where $\frac{d}{dt} = \frac{\partial}{\partial t} + \frac{\partial\psi}{\partial x}\frac{\partial}{\partial y} - \frac{\partial\psi}{\partial y}\frac{\partial}{\partial x}$.

Perturbation Equation

In the large-scale, quasi-geostrophic motion a rotating layer of homogeneous incompressible and inviscid fluid is considered. If the sphericity of the earth and the bottom topography of the boundary are neglected, then the governing equation of motion, Equation (2.59), takes the following form:

$$\left(\frac{\partial}{\partial t} + \frac{\partial\psi}{\partial x}\frac{\partial}{\partial y} - \frac{\partial\psi}{\partial y}\frac{\partial}{\partial x}\right)\left(\nabla_H^2\,\psi + \frac{1}{\rho_s}\frac{\partial}{\partial z}\left(\frac{\rho_s}{S}\ \frac{\partial\psi}{\partial z}\right)\right) = 0; \tag{2.70}$$

and the equations for the boundaries, Equations (2.67) through (2.69), are reduced to this simple equation

$$\left(\frac{\partial}{\partial t} + \frac{\partial\psi}{\partial x}\frac{\partial}{\partial y} - \frac{\partial\psi}{\partial y}\frac{\partial}{\partial x}\right)\frac{\partial\psi}{\partial z} = 0 \quad \text{at } z = 0,1. \tag{2.71}$$

The initial state flow is usually considered as a zonal flow (i.e., along latitude circle). The stream function in this basic state is denoted by $\psi = \psi_0(y,z)$. The velocity (U_0) and the potential temperature (θ_0) are represented respectively by

$$U_0(y,z) = -\,\partial\phi_0/\partial y \tag{2.72}$$

$$\theta_0(y,z) = \partial\phi_0/\partial z. \tag{2.73}$$

According to Equation (2.57), the thermal wind relation is given by

$$\partial U_0/\partial z = -\,\partial\theta_0/\partial y. \tag{2.74}$$

After perturbation, the stream function in the perturbed state must be characterized by the following two parts:

$$\psi(x,y,z,t) = \psi_0(y,z) + \phi(x,y,z,t) \tag{2.75}$$

where ϕ represents the perturbation of the initial state. Differentiating Equation (2.75) with respect to x,y,z, respectively, and applying the relations of Equations (2.72) through (2.74), we have the following expressions:

$$\frac{\partial\psi}{\partial x} = \frac{\partial\phi}{\partial x} \tag{2.76}$$

$$\frac{\partial\psi}{\partial y} = -U_0 + \frac{\partial\phi}{\partial y} \tag{2.77}$$

$$\frac{\partial\psi}{\partial z} = \theta_0 + \frac{\partial\phi}{\partial z} \tag{2.78}$$

$$\frac{\partial^2\psi}{\partial x^2} = \frac{\partial^2\phi}{\partial x^2} \tag{2.79}$$

$$\frac{\partial^2\psi}{\partial y^2} = -\frac{\partial U_0}{\partial y} + \frac{\partial^2\phi}{\partial y^2}\,. \tag{2.80}$$

Substituting the above five expressions into Equation (2.70) with the aid of Equation (2.73) gives the following nonlinear partial differential equation:

$$\left(\frac{\partial}{\partial t} + U_0\frac{\partial}{\partial x}\right) q + \frac{\partial\phi}{\partial x}\frac{\partial\Pi}{\partial y} + J(\phi,q) = 0 \tag{2.81}$$

where $\quad q = \dfrac{\partial^2\phi}{\partial x^2} + \dfrac{\partial^2\phi}{\partial y^2} + \dfrac{1}{\rho_s}\dfrac{\partial}{\partial z}\left(\dfrac{\rho_s}{S}\dfrac{\partial\phi}{\partial z}\right)$

$\quad = $ perturbation potential vorticity

$$\Pi = \frac{\partial^2 \psi_0}{\partial y^2} + \frac{1}{\rho_s} \frac{\partial}{\partial z} \left(\frac{\rho_s}{S} \frac{\partial \psi_0}{\partial z} \right)$$

= basic state potential vorticity

$$\frac{\partial \Pi}{\partial y} = - \frac{\partial^2 U_0}{\partial y^2} - \frac{1}{\rho_s} \frac{\partial}{\partial z} \left(\frac{\rho_s}{S} \frac{\partial U_0}{\partial z} \right)$$

= potential vorticity gradient for the basic flow

$J(\phi,q) = \frac{\partial(\phi,q)}{\partial(x,y)}$ = Jacobian operator for x and y.

For the boundary condition in the y direction, we assume that the rigid walls exist at $y = \pm 1$, containing the region of the flow and the perturbations. Under this condition, it follows that the velocity, v, has to vanish on $Y = \pm 1$, i.e.,

$$\frac{\partial \phi}{\partial x} = 0 \quad \text{at } y = \pm 1, \tag{2.82}$$

and the average of the velocity, u, is independent of time at rigid walls, i.e.,

$$\frac{\partial}{\partial t} \left\langle \frac{\partial \phi}{\partial y} \right\rangle = 0 \quad \text{at } y = \pm 1 \tag{2.83}$$

where $\left\langle \frac{\partial \phi}{\partial y} \right\rangle = \lim_{X \to \infty} \frac{1}{2X} \int_{-X}^{X} \frac{\partial \phi}{\partial y} dx.$

For the boundary condition in the z direction, substituting Equations (2.72) and (2.76) through (2.80) into Equation (2.71) yields

$$\left(\frac{\partial}{\partial t} + U_0 \frac{\partial}{\partial x} \right) \frac{\partial \phi}{\partial z} - \frac{\partial U_0}{\partial z} \frac{\partial \phi}{\partial x} + J\left(\phi, \frac{\partial \phi}{\partial z} \right) = 0. \tag{2.84}$$

Linear Stability Problem

If the nonlinear terms are dropped from Equations (2.81) and (2.84) with the assumptions of constant ρ_s, S, and $U_0 = z$, then the so-called linear stability problem or Eady problem [21] is expressed by the following form,

$$\left(\frac{\partial}{\partial t} + z\frac{\partial}{\partial x}\right)\left(\frac{\partial^2\phi}{\partial x^2} + \frac{\partial^2\phi}{\partial y^2} + \frac{1}{S}\frac{\partial^2\phi}{\partial z^2}\right) = 0 \tag{2.85}$$

and the boundary conditions become

$$\left(\frac{\partial}{\partial t} + z\frac{\partial}{\partial x}\right)\frac{\partial\phi}{\partial z} - \frac{\partial\phi}{\partial x} = 0 \quad \text{at } z = 0,1. \tag{2.86}$$

The solution to the linear Equation (2.85) which is consistent with the boundary conditions, Equations (2.82) and (2.83), is represented by [21]

$$\phi(x,y,z,t) = A(z)\cos\left(n + \frac{1}{2}\right)\pi y \exp\left(ik(x - ct)\right) \quad \text{for } i = \sqrt{-1}$$

where $n = 0,1,2,\ldots.$

Using this solution form, Equation (2.85) is reduced to the ordinary differential equation

$$(z - c)\left(\frac{d^2A}{dz^2} - \mu^2 A\right) = 0 \tag{2.87}$$

where $\mu^2 = \left(k^2 + \left(n + \frac{1}{2}\right)^2 \pi^2\right)S.$

The boundary Equation (2.86) is also reduced to

$$(z - c)\frac{dA}{dz} - A = 0 \quad \text{at } z = 0,1. \tag{2.88}$$

If $(z - c)$ is not equal to zero, the solution to Equation (2.87) is

$A(z) = a \cosh \mu z + b \sinh \mu z$

where a and b are constants.

Applying solution A(z) to the boundary Equation (2.88) gives

$$c^2 - c + \mu^{-1}\coth \mu - \mu^{-2} = 0. \qquad (2.89)$$

Solving this quadratic equation yields

$$c = \frac{1}{2} \pm \frac{1}{\mu}\left[\left(\frac{\mu}{2} - \coth\frac{\mu}{2}\right)\left(\frac{\mu}{2} - \tanh\frac{\mu}{2}\right)\right]^{\frac{1}{2}}.$$

The above condition shows that a critical value of μ exists and it is $\mu_c = 2.3994$.

When $\mu < \mu_c$, c has two complex roots which are associated with the stability and the instability of the linear Eady problem. Finally, the solution to Equation (2.85) can be written in the following form:

$$\phi(x,y,z,t) = \exp\,(ik(x - ct)) \cos\,(n + \tfrac{1}{2})\,\pi y(a \cosh \mu z + b \sinh \mu z),$$

where n = 0,1,2,..., a and b are constants.

Nonlinear Stability Problem

If the same assumptions concerning the basic state employed in the linear problem are used again in Equation (2.81), then this equation has the following form:

$$\left(\frac{\partial}{\partial t} + z\,\frac{\partial}{\partial x}\right) q = \frac{\partial \phi}{\partial y}\frac{\partial q}{\partial x} - \frac{\partial \phi}{\partial x}\frac{\partial q}{\partial y} \qquad (2.90)$$

where $q = \dfrac{\partial^2 \phi}{\partial x^2} + \dfrac{\partial^2 \phi}{\partial y^2} + \dfrac{1}{S}\dfrac{\partial^2 \phi}{\partial z^2}$.

Equation (2.90) is a full nonlinear problem in the interior of a baroclinic flow. The baroclinic instability of an infinite fluid on f-plane was investigated in the Eady problem without potential vorticity. If the assumption of potential vorticity being zero initially should be retained, and according to Equation (2.9) the potential vorticity should be zero for all times, then the interior equation for pressure perturbation (ϕ) takes the following form:

$$\frac{\partial^2 \phi}{\partial x^2} + \frac{\partial^2 \phi}{\partial y^2} + \frac{1}{S} \frac{\partial^2 \phi}{\partial z^2} = 0 \tag{2.91}$$

where the stratification parameter, S, is a specified external parameter. Note that with the assumption of vanishing potential vorticity, the governing differential Equation (2.90) is rendered linear.

The boundary condition in the y direction is unaltered; but in the z direction, it changes from Equation (2.84) with $U_0 = z$ into the following expression:

$$\frac{\partial}{\partial t} \left[\frac{\partial \phi}{\partial z}\right] = \frac{\partial}{\partial x} \left[\phi - z \frac{\partial \phi}{\partial z} + \frac{\partial \phi}{\partial y} \frac{\partial \phi}{\partial z}\right] - \frac{\partial}{\partial y} \left[\frac{\partial \phi}{\partial x} \frac{\partial \phi}{\partial z}\right] \tag{2.92}$$

This equation for the boundary conditions is nonlinear and complicated. Both Equations (2.91) and (2.92) constitute the nonlinear stability problem in the present study. Note that in the present, the nonlinearity is in the boundary conditions and not in the field equations.

CHAPTER III

SOLUTION METHOD

Spectral Method

The previous chapter has presented the formulation of a nonlinear problem for the purpose of this study. Since the analytical or closed-form solution is not obtainable, it is necessary to make use of the numerical techniques. In principle there are three basic numerical methods used to solve the partial differential equations: 1) finite difference methods, 2) finite element methods, and 3) spectral methods. In the past years, weather prediction [28] was treated by the finite difference methods. Recently the finite element technique has also been used in atmospheric science [29,30]. Since the publication of the 1977 monograph [31], the spectral method has been applied to meteorology [32,33] because it is particularly useful in numerical geophysical fluid dynamics. It is also used to solve the problems of fluid dynamics in both the incompressible and the compressible flows [34,35,36,37].

There are three ways to apply the spectral methods to the engineering problems; namely, the Galerkin approximation, the tau approximation, and the collocation (or pseudospectral) approximation [31]. The basic idea of the spectral method is given below. Consider the differential equation,

$$\frac{\partial u}{\partial t} = G(u), \tag{3.1}$$

over a spatial domain, D, with suitable boundary conditions on u along the domain boundary. Here u is a function of independent variables x and t. It is possible to approximate u by f in the following finite series form:

$$f(x,t) = \sum_{j=1}^{N} a_j(t)\, F_j(x) \tag{3.2}$$

where $F_j(x)$ are the linearly independent basis functions and $a_j(t)$ are the coefficients which are functions of time t. Substituting Equation (3.2) into (3.1) yields the difference $\partial f/\partial t - G(f)$. The integration of this difference over domain, D, with F_j as weighting functions must be zero in the following manner:

$$\int_D \left[\frac{\partial f}{\partial t} - G(f)\right] F_k\, dx = 0. \tag{3.3}$$

Thus, a system of N equations for N unknowns, da_k/dt, is obtained from these integrals. The important difference between Galerkin and tau approximations is that the functions F_j should satisfy the boundary conditions in the Galerkin method, but they need not in the tau method. The boundary constraints are imposed as part of the conditions to determine the expansion coefficients a_k. The collocation approximation will be introduced in the following section.

Pseudospectral Method

In the present investigation, the pseudospectral method is chosen because the collocation approximation is the easiest and most efficient method to apply to our nonlinear problem. The boundary conditions are also easier to apply because the collocation method involves solving the equations by using the discrete Fourier transforms and fast transforms.

The following analysis is concentrated on the spectral collocation method. The standard collocation points in the two-dimensional case are

$$x_n = 2\pi n/N, \quad n = 0,1,\ldots, (N - 1) \tag{3.4}$$

$$y_m = 2\pi m/M, \quad m = 0,1,\ldots, (M - 1). \tag{3.5}$$

The perturbation function and its derivatives are approximated by $\phi(x_n,y_m,z)$, $\phi_x(x_n,y_m,z)$, $\phi_y(x_n,y_m,z)$, and $\phi_z(x_n,y_m,z)$, respectively. So the spatial discretization of the equation for the boundary conditions, Equation (2.92), is given by

$$\partial\phi_z(x_n,y_m,z)/\partial t = \partial F/\partial x - \partial G/\partial y, \tag{3.6}$$

where $F = \phi - z\phi_z + \phi_y\phi_z$ and $G = \phi_x\phi_z$. The solutions to Equation (3.6) are constructed by using the discrete Fourier transform (DFT) or the fast Fourier transform (FFT) on the right-hand side, and the Runge-Kutta method, leapfrog method, or the Adams-Bashforth method for time integration on the left-hand side.

Concerning stability and convergence of the pseudospectral Fourier method [38], consider the solution of the time-dependent initial value problem

$$\frac{\partial u}{\partial t} = Lu \tag{3.7}$$

with initial condition $u(t = 0) = u_0$. Here u is a function of x and t, L is a linear differential operator. The collocation approximation gives

$$\frac{\partial u_N}{\partial t} = L_N u_N \tag{3.8}$$

where u_N and L_N approximate to u and L, respectively. This approximation is said to be consistent and convergent if the norms of $(L - L_N)u$ and $(u(t) - u_N(t))$ approach zero as N approaches infinity, respectively. The pseudospectral method is said to be stable if

$$\| u_N(t) \| \leq C \|u_N(0)\| \quad \text{for } 0 \leq t \leq T. \tag{3.9}$$

Here T is the final time, and C is a constant dependent on T, but not on N.

For time integration, the fourth order Runge-Kutta method is fourth-order accurate, but has the disadvantage of requiring computation and evaluation of the derivatives of function such as f(t,x) [39].

The leapfrog method is one-step, explicity, three-time level, and second-order accurate in space and time, but it needs another method to find the first two-time numerical computation [40].

In practical applications of the pseudospectral approach, it has been found that the Adams-Bashforth time integration scheme works well [41]. So this method is used in time integration. The time step size in this case is suggested [31] with the condition,

$$\Delta t \leq \frac{8}{N^2}, \tag{3.10}$$

for stability. Here N is the number of collocation points or grid points along the x direction.

Discrete Fourier Transforms

The complex Fourier series [42] may be considered as a transformation that maps an analytical function to a sequence of Fourier series coefficients. This function, f(t), is expressed by

$$f(t) = \sum_{k=-\infty}^{\infty} C_k \, e^{2\pi ikt/T} \tag{3.11}$$

with the coefficient, C_k, given by

$$C_k = \frac{1}{T} \int_{-\frac{T}{2}}^{\frac{T}{2}} f(t) \, e^{-2\pi ikt/T} dt \tag{3.12}$$

where T is the period.

The Fourier transform [43,44] is a mapping that changes a function, f(t), into another function, F(w). The one-dimensional Fourier transform pair is defined as

$$F(w) = \int_{-\infty}^{\infty} f(t) \, e^{-2\pi iwt} dt \tag{3.13}$$

$$f(t) = \int_{-\infty}^{\infty} F(w) \, e^{2\pi iwt} dw. \tag{3.14}$$

The former is called the (direct) Fourier transform while the latter is known as the inverse Fourier transform. Similarly, the two-dimensional Fourier transform pair for the function f(x,y) is represented by

$$F(u,v) = \int_{-\infty}^{\infty}\int_{-\infty}^{\infty} f(x,y)\, e^{-2\pi i(ux + vy)} dxdy \tag{3.15}$$

$$f(x,y) = \int_{-\infty}^{\infty}\int_{-\infty}^{\infty} F(u,v)\, e^{2\pi i(ux + vy)} dudv. \tag{3.16}$$

To determine either the Fourier series or the Fourier transforms of functions, integrals must be evaluated with the infinite limits. Sometimes these functions are so complicated that the numerical computation is needed. Sampling and truncating the functions makes the computer digest sequences of numbers which represent the given function. The DFT is a right operation that maps a finite sequence $\{f(k)\}$ to another finite sequence $\{F(j)\}$. The DFT pair is defined as

$$F(j) = \sum_{k=0}^{N-1} f(k)\, W^{-kj},\ j = 0,1,\ldots, N-1 \tag{3.17}$$

$$f(k) = \frac{1}{N}\sum_{j=0}^{N-1} F(j)\, W^{kj},\ k = 0,1,\ldots, N-1 \tag{3.18}$$

where $W = \exp(2\pi i/N)$ is called the weighting kernel [42]. This kernel possesses some basic properties as follows:

$W^{\pm kN} = 1$ for any integer k;

$W^{k\pm j} = W^k W^{\pm j}$;

$W^{k(N\pm j)} = W^{\pm kj}$, N is the period for cycle.

If N is equal to 8, k and j vary from 0 to N - 1, then W^{kj} represents a symmetric matrix as illustrated in Table 4, and has the cyclical nature of process shown in Figure 6.

Table 4. Values of W^{kj} for N = 8.

j \ k	0	1	2	3	4	5	6	7
0	W^0	W^0	W^0	W^0	W^0	W^0	W^0	W^0
1	W^0	W^1	W^2	W^3	W^4	W^5	W^6	W^7
2	W^0	W^2	W^4	W^6	W^0	W^2	W^4	W^6
3	W^0	W^3	W^6	W^1	W^4	W^7	W^2	W^5
4	W^0	W^4	W^0	W^4	W^0	W^4	W^0	W^4
5	W^0	W^5	W^2	W^7	W^4	W^1	W^6	W^3
6	W^0	W^6	W^4	W^2	W^0	W^6	W^4	W^2
7	W^0	W^7	W^6	W^5	W^4	W^3	W^2	W^1

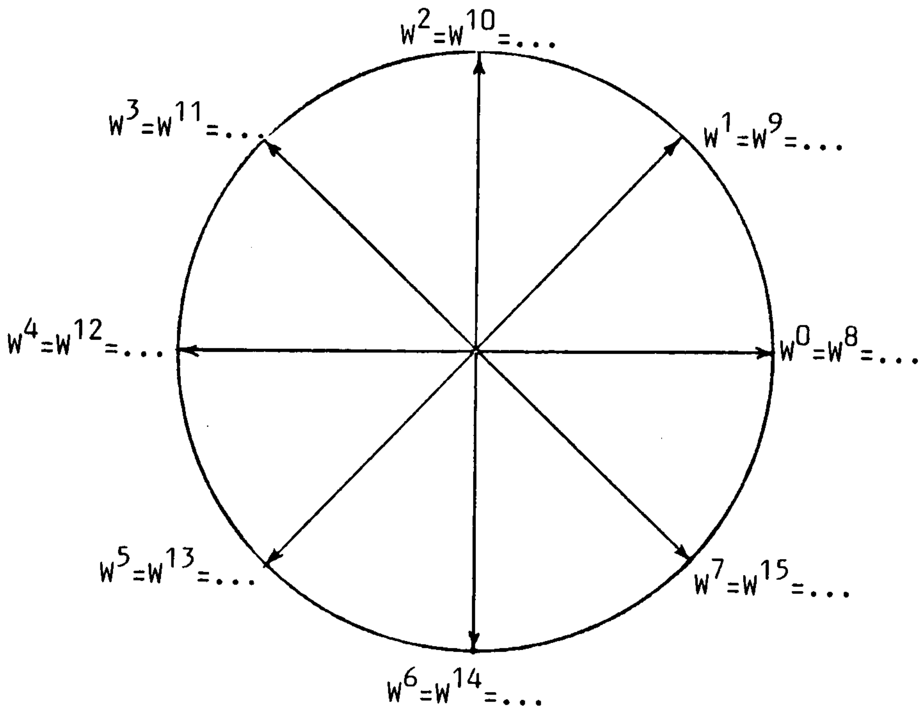

Figure 6. Cyclic Nature of W^{kj} for N = 8.

In the case of our study, k will range from negative to positive values while $j = 0,1,\ldots, N - 1$. Here N must be an odd number for the sake of matching between k and j. If $N = 7$, then the matrix W^{kj}, indicated in Table 5, is not symmetric for $-3 \leq k \leq 3$ and $0 \leq j \leq 7$.

For the two-dimensional case, the DFT pair is defined as the following expressions:

$$F(u,v) = \sum_{x=0}^{N-1} \sum_{y=0}^{M-1} f(x,y)\, W_N^{-ux}\, W_M^{-vy} \tag{3.19}$$

$$f(x,y) = \frac{1}{NM} \sum_{u=0}^{N-1} \sum_{v=0}^{M-1} F(u,v)\, W_N^{ux}\, W_M^{vy} \tag{3.20}$$

where $W_N = \exp\,(2\pi i/N)$

$W_M = \exp\,(2\pi i/M)$.

The above two equations for the two-dimensional DFT pair will be applied to the problem in Chapter IV.

Fast Transform

Concerning the FFT, it is an algorithm [45] for computing the DFT of a function with minimum CPU time because the computing time will be reduced from N^2 (for one-dimensional DFT) to a time proportional to $N \log_2 N$. If N is an even number, particularly $N = 2^p$ and p is a positive integer, the FFT is applicable. In the present case, owing to the odd number N, another fast transform should be used in Chapter IV to reduce computer CPU time.

Table 5. Values of W^{kj} for N = 7.

j \ k	-3	-2	-1	0	1	2	3
0	W^0	W^0	W^0	W^0	W^0	W^0	W^0
1	W^{-3}	W^{-2}	W^{-1}	W^0	W^1	W^2	W^3
2	W^{-6}	W^{-4}	W^{-2}	W^0	W^2	W^4	W^6
3	W^{-2}	W^{-6}	W^{-3}	W^0	W^3	W^6	W^2
4	W^{-5}	W^{-1}	W^{-4}	W^0	W^4	W^1	W^5
5	W^{-1}	W^{-3}	W^{-5}	W^0	W^5	W^3	W^1
6	W^{-4}	W^{-5}	W^{-6}	W^0	W^6	W^5	W^4

CHAPTER IV

NUMERICAL PROCEDURE

Features of Solution Form

In Chapter II, the nonlinear problem consists of the following equations: 1) the linear equation for perturbation pressure,

$$\frac{\partial^2 \phi}{\partial x^2} + \frac{\partial^2 \phi}{\partial y^2} + \frac{1}{S}\frac{\partial^2 \phi}{\partial z^2} = 0 \qquad (4.1)$$

where S = 1 in the present case;

2) the equation for the boundary conditions in the y direction,

$$\frac{\partial \phi}{\partial x} = 0 \quad \text{at } y = 0,b \qquad (4.2)$$

where b = 3.14 in the present case;

and 3) the nonlinear equation for the boundary conditions in the z direction,

$$\frac{\partial}{\partial t}\left(\frac{\partial \phi}{\partial z}\right) = \frac{\partial F}{\partial x} - \frac{\partial G}{\partial y} \quad \text{at } z = 0,1 \qquad (4.3)$$

where

$$F = \phi - z\frac{\partial \phi}{\partial z} + \frac{\partial \phi}{\partial y}\frac{\partial \phi}{\partial z}$$

$$G = \frac{\partial \phi}{\partial x}\frac{\partial \phi}{\partial z}.$$

The solution to this problem is considered to have the following form:

$$\phi = \sum_{k=-k}^{K} \sum_{l=-k}^{K} e^{i(kx + ly)} (A \cosh Kz' + B \sinh Kz') \qquad (4.4)$$

where $\phi = \phi(x,y,z,t)$

$A = A(k,l,t)$

$B = B(k,l,t)$

$K = \sqrt{k^2 + l^2}$

$z' = z - 1/2.$

Here the limit of z' is (-1/2, 1/2) as z goes from 0 to 1 for the convenience of the numerical computation.

The wave amplitudes A(k,l) and B(k,l) are complex functions of time. Their conjugate complexes are A* and B*. Since K equals definite real values, regardless of k and l being positive or negative, both cosh Kz' and sinh Kz' do not affect the complex forms of A, B, and their conjugates. Therefore, ϕ can be split into the following two parts:

$$\phi = \phi_A + \phi_B \tag{4.5}$$

where

$$\phi_A = \sum_k \sum_l e^{i(kx + ly)} A \cosh Kz' \tag{4.6}$$

$$\phi_B = \sum_k \sum_l e^{i(kx + ly)} B \sinh Kz' \quad \text{for } -K \leq k,l \leq K. \tag{4.7}$$

If setting $A^+ = A(k,l)$, $A^- = A(-k,-l)$, and $p = kx + ly$, then the expression of ϕ_A can be written simply and without loss of generality in the following form:

$$\phi_A = A^+ \exp(ip) + A^- \exp(-ip)$$

$$= (A_r^+ + iA_i^+)(\cos p + i \sin p) + (A_r^- + iA_i^-)(\cos p - i \sin p)$$

$$= (A_r^+ + A_r^-) \cos p + (A_i^- - A_i^+) \sin p$$

$$+ i \left[(A_i^+ + A_i^-) \cos p + (A_r^+ - A_r^-) \sin p \right]. \tag{4.8}$$

In order to make ϕ_A real, the imaginary part of Equation (4.8) must be zero. Therefore, $A_r^- = A_r^+$, and $A_i^- = -A_i^+$, that is

$$A(-k,-l) = A^*(k,l) \tag{4.9}$$

and

$$A(k,-l) = A^*(-k,l). \tag{4.10}$$

Similarly, the following expressions can be found:

$$B(-k,-l) = B^*(k,l) \tag{4.11}$$

and

$$B(k,-l) = B^*(-k,l). \tag{4.12}$$

The relationships of Equations (4.9) through (4.12) are illustrated in Figure 7, and they are useful to reduce half as much as the number of the numerical computation.

Analysis of Boundary Conditions

The boundary conditions play an important role in the analysis of the pseudospectral method. Once the solution ϕ is given, the non-linear partial differential Equation (4.3) for boundary conditions can be reduced to ordinary differential equations through which both coefficients A and B will be obtained from the time integration.

Differentiating ϕ with respect to x, y, and z', respectively, the following expressions can be obtained:

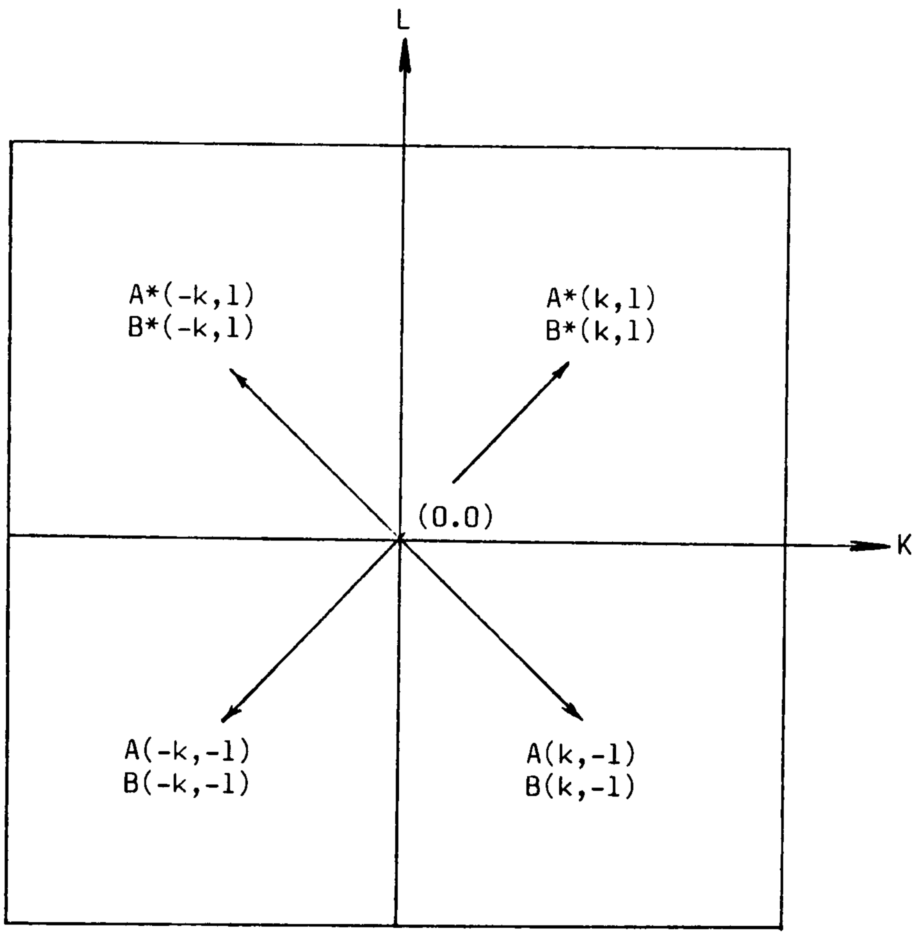

Figure 7. Regions of Relationship Between A, B and A*, B*.

$$\phi_x = \frac{\partial\phi}{\partial x} = \sum_k \sum_l ike^{i(kx + ly)}(A \cosh Kz' + B \sinh Kz') \tag{4.13}$$

$$\phi_y = \frac{\partial\phi}{\partial y} = \sum_k \sum_l ile^{i(kx + ly)}(A \cosh Kz' + B \sinh Kz') \tag{4.14}$$

$$\phi_z = \frac{\partial\phi}{\partial z'} = \sum_k \sum_l Ke^{i(kx + ly)}(B \cosh Kz' + A \sinh Kz') \tag{4.15}$$

where $\partial\phi/\partial z' = \partial\phi/\partial z = \phi_z$.

Taking the derivative of $\partial\phi/\partial z'$ with respect to t yields

$$\frac{\partial\phi_z}{\partial t} = \sum_k \sum_l Ke^{i(kx + ly)} \left(\frac{dB}{dt} \cosh Kz' + \frac{dA}{dt} \sinh Kz'\right). \tag{4.16}$$

Substituting Equations (4.13) through (4.16) into Equation (4.3) gives

$$\sum_k \sum_l Ke^{i(kx + ly)} \left(\frac{dB}{dt} \cosh \frac{K}{2} \pm \frac{dA}{dt} \sinh \frac{K}{2}\right) = \frac{\partial F}{\partial x} - \frac{\partial G}{\partial t} \quad \text{at } z' = \pm \frac{1}{2}. \tag{4.17}$$

Multiplying both sides of Equation (4.17) by $e^{-i(kx + ly)}$ and integrating by parts with respect to x and y, the following expressions are obtained:

$$K\left(\frac{dB}{dt} \cosh \frac{K}{2} \pm \frac{dA}{dt} \sinh \frac{K}{2}\right)$$

$$= \frac{1}{b}\frac{1}{b}\int_0^b\int_0^b e^{-i(kx + ly)}\left(\frac{\partial F}{\partial x} - \frac{\partial G}{\partial y}\right)dxdy$$

$$= ikF(k,l) - ilG(k,l) = \theta_{\pm}(k,l) \text{ at } z' = \pm \frac{1}{2}, \tag{4.18}$$

where

$$F(k,l) = \frac{1}{b^2} \int_0^b \int_0^b e^{-i(kx + ly)} F \, dxdy \tag{4.19}$$

$$G(k,l) = \frac{1}{b^2} \int_0^b \int_0^b e^{-i(kx + ly)} G \, dxdy. \tag{4.20}$$

Thus, the following two equations are obtained:

$$\frac{dB}{dt} K \cosh \frac{K}{2} + \frac{dA}{dt} K \sinh \frac{K}{2} = \theta_+(k,l) \tag{4.21}$$

$$\frac{dB}{dt} K \cosh \frac{K}{2} - \frac{dA}{dt} K \sinh \frac{K}{2} = \theta_-(k,l). \tag{4.22}$$

Solving these two equations yields

$$\frac{dA}{dt} = \frac{\theta_+(k,l) - \theta_-(k,l)}{2 \ K \sinh \ (K/2)} \tag{4.23}$$

$$\frac{dB}{dt} = \frac{\theta_+(k,l) + \theta_-(k,l)}{2 \ K \cosh \ (K/2)} . \tag{4.24}$$

They are simultaneously ordinary differential equations. Both coefficients A and B can be obtained by time integration.

Transformation of ϕ and Its Derivatives

In Chapter III, the basic ideas of the transformations were presented. First, the discrete transforms are applied to the calculation of sequences for ϕ and its derivatives ϕ_x, ϕ_y, and ϕ_z to get the DFT of F and G in Equation (4.3). Then applying the inverse DFT to computation of double integrations gives the results for F(k,l) and G(k,l) from which $\theta_+(k,l)$ and $\theta_-(k,l)$ may be found. In the course of these transforms, the FFT technique could be used to reduce the number of computation.

DFT of ϕ and Its Derivatives

Applying the DFT technique to Equation (4.4) yields the following expressions:

$$\phi(n,m) = \sum_k \sum_l \left[A \cosh \frac{K}{2} \pm B \sinh \frac{K}{2}\right] e^{2\pi i\left(\frac{kn}{N} + \frac{lm}{M}\right)}$$

$$= \sum_k \sum_l a(k,l)\, W_N^{kn}\, W_M^{lm},$$

$$\text{for } k = -\frac{N-1}{2}, -\frac{N-3}{2}, \ldots, \frac{N-1}{2}$$

$$l = -\frac{M-1}{2}, -\frac{M-3}{2}, \ldots, \frac{M-1}{2}$$

$$n = 0,1,\ldots,N-1$$

$$m = 0,1,\ldots,M-1 \tag{4.25}$$

where $a(k,l) = A \cosh (K/2) \pm B \sinh (K/2)$

$W_N = \exp (2\pi i/N)$ = weighting kernel for N

$W_M = \exp (2\pi i/M)$ = weighting kernel for M

N = number of grid points in x direction

M = number of grid points in y direction.

Since both k and l range from negative to positive values while both n and m are positive, special attention must be paid to matching the corresponding nodes in the implementation of the computing program. Figure 8 shows the matching of the points $(-\frac{N-1}{2}, -\frac{M-1}{2})$, $(-\frac{N-1}{2}, \frac{M-1}{2})$, $(\frac{N-1}{2}, \frac{M-1}{2})$, and $(\frac{N-1}{2}, -\frac{M-1}{2})$ in the wavenumber plane corresponding to the points (0, 0), (0, M-1), (N-1, M-1), and (N-1, 0) in the physical plane.

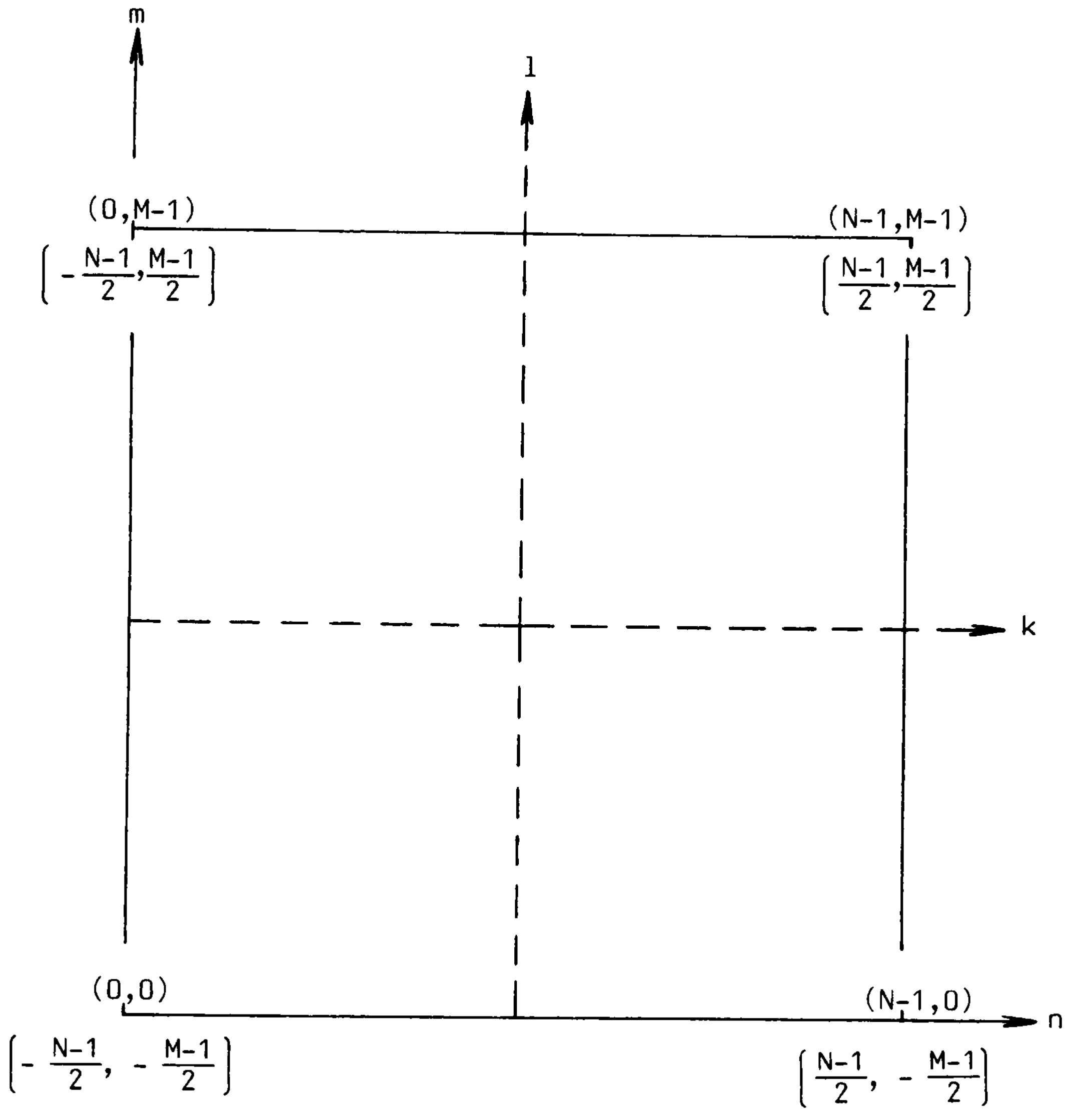

$$k = -\frac{N-1}{2},\ -\frac{N-3}{2},\ldots,0,\ldots,\frac{N-1}{2}$$

$$l = -\frac{M-1}{2},\ -\frac{M-3}{2},\ldots,0,\ldots,\frac{M-1}{2}$$

$$n = 0,1,\ldots,N-1$$

$$m = 0,1,\ldots,M-1$$

Figure 8. The k,l Plane Matching with the n,m Plane.

Similarly the DFTs for ϕ_x, ϕ_y, and ϕ_z are given by

$$\phi_x(n,m) = \sum_k \sum_l ika(k,l)\, W_N^{kn}\, W_M^{lm} \tag{4.26}$$

$$\phi_y(n,m) = \sum_k \sum_l ila(k,l)\, W_N^{kn}\, W_M^{lm} \tag{4.27}$$

$$\phi_z(n,m) = \sum_k \sum_l Ka'(k,l)\, W_N^{kn}\, W_M^{lm} \tag{4.28}$$

where $a'(k,l)$ differs from $a(k,l)$, and $a'(k,l) = B \cosh (K/2) \pm A \sinh (K/2)$.

For the numerical calculation, Equation (4.3), with the aid of Equations (4.25) through (4.28), is used to compute the DFTs of F and G. Both of them are given by

$$F(n,m) = \phi(n,m) - [z - \phi_y(n,m)]\, \phi_z(n,m) \tag{4.29}$$

$$G(n,m) = \phi_x(n,m)\, \phi_z(n,m). \tag{4.30}$$

<u>Inverse DFT of F(n,m) and G(n,m)</u>

According to Equations (3.19) and (3.20), the inverse DFTs of F(n,m) and G(n,m) for these double integral Equations (4.19) and (4.20) are given by

$$F(k,l) = \frac{1}{N}\frac{1}{M} \sum_{n=0}^{N-1} \sum_{m=0}^{M-1} \frac{F(n,m)}{b^2}\, W_N^{-kn}\, W_M^{-lm} \tag{4.31}$$

$$G(k,l) = \frac{1}{N}\frac{1}{M} \sum_{n=0}^{N-1} \sum_{m=0}^{M-1} \frac{G(n,m)}{b^2}\, W_N^{-kn}\, W_M^{-lm} \tag{4.32}$$

where $k = -\frac{N-1}{2}, -\frac{N-3}{2}, \ldots, \frac{N-1}{2}$

$l = -\frac{M-1}{2}, -\frac{M-3}{2}, \ldots, \frac{M-1}{2}$

$$W_N = \exp\,(2\pi i/N)$$

$$W_M = \exp\,(2\pi i/M).$$

Once $F(k,l)$ and $G(k,l)$ have been determined, $\frac{dA}{dt}$ and $\frac{dB}{dt}$ can be found from Equation (4.18), and Equations (4.21) through (4.24).

Fast Transformation

To compute $\phi(n,m)$ in Equation (4.25), the double summation should be directly or indirectly expanded. If the direct technique is taken, the summation is expressed by

$$\begin{aligned}\phi(n,m) = {} & a\left(-\frac{N-1}{2},\ -\frac{M-1}{2}\right) W_N^{-\left(\frac{N-1}{2}\right)n}\ W_M^{-\left(\frac{M-1}{2}\right)m} + \cdots \\ & + a\left(-\frac{N-1}{2},\ \frac{M-1}{2}\right) W_N^{-\left(\frac{N-1}{2}\right)n}\ W_M^{\left(\frac{M-1}{2}\right)m} + \cdots \\ & + a\left(\frac{N-1}{2},\ -\frac{M-1}{2}\right) W_N^{\left(\frac{N-1}{2}\right)n}\ W_M^{-\left(\frac{M-1}{2}\right)m} + \cdots \\ & + a\left(\frac{N-1}{2},\ \frac{M-1}{2}\right) W_N^{\left(\frac{N-1}{2}\right)n}\ W_M^{\left(\frac{M-1}{2}\right)m}\,. \end{aligned} \tag{4.33}$$

If the indirect technique [46] is taken, the double summation is split into two parts as follows:

$$b(k,m) = \sum_{l} a(k,l)\, W_M^{lm} \tag{4.34}$$

$$\phi(n,m) = \sum_{k} b(k,m)\, W_N^{kn}. \tag{4.35}$$

Here each part is treated as a one-dimensional case. The summation of the right-hand side of each part is done by l or k, respectively.

From Equation (4.33), the total number of multiplication is (NM) (NM) = $(NM)^2$. However, in Equations (4.34) and (4.35) it is found that the total number of multiplication is the sum of (NM)M and (NM)N equal to (NM) (N + M). If both N and M are larger than 2, the indirect technique can save the computing time because of $(NM)(N + M) < (NM)^2$. If N and M are equal to 2^p and p is an integer, then the FFT is very useful in computing this transform which requires, roughly, $N \log_2 N$ operations [45]. However, the FFT method is replaced by the technique to separate the two-dimensional transform into two one-dimensional transforms in the present study. So the indirect technique is used for all the transforms such as F(n,m), G(n,m), F(k,l), and G(k,l) in this computation. In fact, this technique is a matrix method which will be illustrated in the following section.

Computing $\phi(n,m)$

If Equation (4.33) is used to compute $\phi(n,m)$ for $0 \leq n \leq N - 1$ and $0 \leq m \leq M - 1$, then it can be replaced by the following matrix form:

$$\Phi = LAR \tag{4.36}$$

where

$$\Phi = \begin{bmatrix} \phi(0,0) & \phi(0,1) & \cdots & \phi(0, M-1) \\ \phi(1,0) & \phi(1,1) & \cdots & \phi(1, M-1) \\ \cdots & & \cdots & \cdots \\ \phi(N-1, 0) & \phi(N-1, 1) & \cdots & \phi(N-1, M-1) \end{bmatrix}$$

$$L = \begin{bmatrix} W_N^{-\left(\frac{N-1}{2}\right)0} & W_N^{-\left(\frac{N-3}{2}\right)0} & \cdots & W_N^{\left(\frac{N-1}{2}\right)0} \\ W_N^{-\left(\frac{N-1}{2}\right)1} & W_N^{-\left(\frac{N-3}{2}\right)1} & \cdots & W_N^{\left(\frac{N-1}{2}\right)1} \\ \cdots & \cdots & \cdots & \cdots \\ W_N^{-\left(\frac{N-1}{2}\right)(N-1)} & W_N^{-\left(\frac{N-3}{2}\right)(N-1)} & \cdots & W_N^{\left(\frac{N-1}{2}\right)(N-1)} \end{bmatrix}$$

$$A = \begin{bmatrix} a\left(-\frac{N-1}{2}, -\frac{M-1}{2}\right) & a\left(-\frac{N-1}{2}, -\frac{M-3}{2}\right) & \cdots & a\left(-\frac{N-1}{2}, \frac{M-1}{2}\right) \\ a\left(-\frac{N-3}{2}, -\frac{M-1}{2}\right) & a\left(-\frac{N-3}{2}, -\frac{M-3}{2}\right) & \cdots & a\left(-\frac{N-3}{2}, \frac{M-1}{2}\right) \\ \cdots & \cdots & \cdots & \cdots \\ a\left(\frac{N-1}{2}, -\frac{M-1}{2}\right) & a\left(\frac{N-1}{2}, -\frac{M-3}{2}\right) & \cdots & a\left(\frac{N-1}{2}, \frac{M-1}{2}\right) \end{bmatrix}$$

$$R = \begin{bmatrix} W_M^{-\left(\frac{M-1}{2}\right)0} & W_M^{-\left(\frac{M-1}{2}\right)1} & \cdots & W_M^{-\left(\frac{M-1}{2}\right)(M-1)} \\ W_M^{-\left(\frac{M-3}{2}\right)0} & W_M^{-\left(\frac{M-3}{2}\right)1} & \cdots & W_M^{-\left(\frac{M-3}{2}\right)(M-1)} \\ \cdots & \cdots & \cdots & \cdots \\ W_M^{\left(\frac{M-1}{2}\right)0} & W_M^{\left(\frac{M-1}{2}\right)1} & \cdots & W_M^{\left(\frac{M-1}{2}\right)(M-1)} \end{bmatrix}$$

Obviously, Φ is N x M matrix, L is N x N matrix, A is N x M matrix, and R is M x M matrix. If M equals N, k and l vary from -(N-1)/2 to (N-1)/2, then matrix L is the transpose matrix of R, i.e., $L = R^T$. But both matrices L and R are not symmetric. If we set B = AR, then Φ = LB. It means that Φ can be separated into two parts in operation. An illustration with an example is given below.

If M = N = 3 is used and $W_N = W_M = W$ is set, then k = l = -1, 0, 1 and n = m = 0,1,2. With these conditions, Equations (4.34) and (4.35) can be expanded into the following two matrix forms:

$$\begin{bmatrix} b(-1,0) & b(0,0) & b(1,0) \\ b(-1,1) & b(0,1) & b(1,1) \\ b(-1,2) & b(0,2) & b(1,2) \end{bmatrix}$$

$$= \begin{bmatrix} W^{-10} & W^{00} & W^{10} \\ W^{-11} & W^{01} & W^{11} \\ W^{-12} & W^{02} & W^{12} \end{bmatrix} \begin{bmatrix} a(-1,-1) & a(0,-1) & a(1,-1) \\ a(-1,0) & a(0,0) & a(1,0) \\ a(-1,1) & a(0,1) & a(1,1) \end{bmatrix} \qquad (4.37)$$

$$\begin{bmatrix} \phi(0,0) & \phi(0,1) & \phi(0,2) \\ \phi(1,0) & \phi(1,1) & \phi(1,2) \\ \phi(2,0) & \phi(2,1) & \phi(2,2) \end{bmatrix}$$

$$= \begin{bmatrix} W^{-10} & W^{00} & W^{10} \\ W^{-11} & W^{01} & W^{11} \\ W^{-12} & W^{02} & W^{12} \end{bmatrix} \begin{bmatrix} b(-1,0) & b(-1,1) & b(-1,2) \\ b(0,0) & b(0,1) & b(0,2) \\ b(1,0) & b(1,1) & b(1,2) \end{bmatrix} \qquad (4.38)$$

Transposing both sides of Equation (4.37) and substituting the transposed result into Equation (4.38), we obtain the following expression:

$$\Phi_{3x3} = L_{3x3}\, A_{3x3}\, R_{3x3} \tag{4.39}$$

where

$$\Phi_{3x3} = \begin{bmatrix} \phi(0,0) & \phi(0,1) & \phi(0,2) \\ \phi(1,0) & \phi(1,1) & \phi(1,2) \\ \phi(2,0) & \phi(2,1) & \phi(2,2) \end{bmatrix}$$

$$L_{3x3} = \begin{bmatrix} W^{-10} & W^{00} & W^{10} \\ W^{-11} & W^{01} & W^{11} \\ W^{-12} & W^{02} & W^{12} \end{bmatrix}$$

$$A_{3x3} = \begin{bmatrix} a(-1,-1) & a(-1,0) & a(-1,1) \\ a(0,-1) & a(0,0) & a(0,1) \\ a(1,-1) & a(1,0) & a(1,1) \end{bmatrix}$$

$$R_{3x3} = \begin{bmatrix} W^{-10} & W^{-11} & W^{-12} \\ W^{00} & W^{01} & W^{02} \\ W^{10} & W^{11} & W^{12} \end{bmatrix}$$

If $k = l = -1,0,1$ and $n = m = 0,1,2$ is substituted into Equation (4.36) directly, the same result as Equation (4.39) is obtained.

Computation for $\phi(x,y,z,t)$

The perturbation stream function, ϕ, has the features described in the first section of this chapter; but in the process of the computation round-off errors are always introduced. To avoid these errors in the computations, it is necessary to represent the equation for computing $\phi(x,y,z,t)$ in the following real form:

$$\phi(x,y,z,t) = \sum_k \sum_l [(A_r \cosh Kz' + B_r \sinh Kz') \cos (kx + ly)$$

$$- (A_i \cosh Kz' + B_i \sinh Kz') \sin (kx + ly)] \tag{4.40}$$

where A_r = real part of $A(k,l,t)$

A_i = imaginary part of $A(k,l,t)$

B_r = real part of $B(k,l,t)$

B_i = imaginary part of $B(k,l,t)$

$z' = z - 1/2$.

At specific time (t_n), the function of ϕ in three different heights, z, is given below:

Case 1: At ground level ($z = 0$),

$$\phi(x,y,0,t_n) = \sum_k \sum_l [(A_r \cosh \frac{K}{2} - B_r \sinh \frac{K}{2}) \cos (kx + ly)$$

$$- (A_i \cosh \frac{K}{2} - B_i \sinh \frac{K}{2}) \sin (kx + ly)]. \tag{4.41}$$

Case 2: At middle level ($z = 1/2$, or $z^* = 5$ km),

$$\phi(x,y,\frac{1}{2},t_n) = \sum_k \sum_l [A_r \cos (kx + ly) - A_i \sin (kx + ly)] \tag{4.42}$$

where $\cosh (0) = 1$, and $\sinh (0) = 0$.

Case 3: At upper level ($z = 1$, or $z^* = 10$ km),

$$\phi(x,y,1,t_n) = \sum_k \sum_l [(A_r \cosh \frac{K}{2} + B_r \sinh \frac{K}{2}) \cos (kx + ly)$$

$$-(A_i \cosh \frac{K}{2} + B_i \sinh \frac{K}{2}) \sin (kx + ly)]. \tag{4.43}$$

Using the given initial values of A(k,l) and B(k,l), and the computed values of A(k,l) and B(k,l) at specific time, the stream function ϕ can be represented in the physical plane (x,y plane) by the Equations (4.41), (4.42), and (4.43).

Numerical Procedures

From the study of the preceeding sections in this chapter, the procedure for finding wave amplitudes and wave patterns is summarized below:

Step 1: Find derivatives of ϕ at $z' = \pm 1/2$,

$$\phi = \sum_k \sum_l e^{i(kx + ly)} \left(A \cosh \frac{K}{2} \pm B \sinh \frac{K}{2}\right)$$

$$\phi_x = \sum_k \sum_l ike^{i(kx + ly)} \left(A \cosh \frac{K}{2} \pm B \sinh \frac{K}{2}\right)$$

$$\phi_y = \sum_k \sum_l ile^{i(kx + ly)} \left(A \cosh \frac{K}{2} \pm B \sinh \frac{K}{2}\right)$$

$$\phi_z = \sum_k \sum_l ke^{i(kx + ly)} \left(B \cosh \frac{K}{2} \pm A \sinh \frac{K}{2}\right).$$

Step 2: Find DFT of ϕ and its derivatives,

$$\phi(n,m) = \sum_k \sum_l a(k,l)\ W_N^{kn}\ W_M^{lm}$$

$$\phi_x(n,m) = \sum_k \sum_l ika(k,l)\ W_N^{kn}\ W_M^{lm}$$

$$\phi_y(n,m) = \sum_k \sum_l ila(k,l)\ W_N^{kn}\ W_M^{lm}$$

$$\phi_z(n,m) = \sum_k \sum_l Ka'(k,l)\, W_N^{kn}\, W_M^{lm}$$

where

$$a(k,l) = A \cosh (K/2) \pm B \sinh (K/2)$$

$$a'(k,l) = B \cosh (K/2) \pm A \sinh (K/2)$$

$$W_N = \exp(2\pi i/N) \text{ and } W_M = \exp(2\pi i/M).$$

Step 3: Find DFT of F and G,

$$F(n,m) = \phi(n,m) - \begin{bmatrix}1\\0\end{bmatrix} \phi_z(n,m) + \phi_y(n,m)\, \phi_z(n,m)$$

$$G(n,m) = \phi_x(n,m)\, \phi_z(n,m).$$

Step 4: Find inverse DFT of F(n,m) and G(n,m),

$$F(k,l) = \frac{1}{b^2} \frac{1}{NM} \sum_n \sum_m F(n,m)\, W_N^{-kn}\, W_M^{-lm}$$

$$G(k,l) = \frac{1}{b^2} \frac{1}{NM} \sum_n \sum_m G(n,m)\, W_N^{-kn}\, W_M^{-lm}.$$

Step 5: Find $\frac{dA}{dt}$ and $\frac{dB}{dt}$,

$$\frac{dA}{dt} = \frac{\theta_+(k,l) - \theta_-(k,l)}{2K \sinh (K/2)}$$

$$\frac{dB}{dt} = \frac{\theta_+(k,l) + \theta_-(k,l)}{2K \cosh (K/2)} .$$

Step 6: Find new A and B (A and B are given initially) by time integration. Then repeat Steps 2 through 6 for iteration until the final time step.

Step 7: Represent wave patterns at the specific time by Equations (4.41) through (4.43).

CHAPTER V

NUMERICAL RESULTS

Scaling Values and Parameters

In order to solve the nonlinear problem numerically, the relevant scales and parameters necessary in Equations (4.1) and (4.3) need to be specified. In the region of troposphere under investigation, fronts, cyclones, and anti-cyclones are usually formed or created. The atmosphere in this region has the large-scale and circulatory motion. Referring to Tables 2 and 3 in Chapter II, the space and time scales for large-scale atmospheric motion are chosen to have the following values:

Characteristic horizontal length, $L = 1000$ km

Characteristic vertical length, $D = 10$ km

Characteristic horizontal speed, $U = 28$ m/s

Earth's mean radius, $r_0 = 6370$ km.

According to these characteristic values, the following parameters are derived:

Aspect ratio, $\delta = 0.01$

Rossby number, $\varepsilon = 0.19$

Ratio of L to r_0, $L/r_0 = 0.16$

Buoyancy frequency, $N^2 = 10^{-4}\ s^{-2}$

Stratification parameter, $S = 1$.

The first three specified values are also found to satisfy the ordering relationships in Equations (2.33) through (2.35) of Chapter II.

Numerical Integrations

The solution of the nonlinear problem as formulated involves only time integration. In Chapters III and IV, the time integration has been introduced through which the time developments of the wave amplitudes A(k,l) and B(k,l) can be found. The grid points and the physical plane size are necessary for the application of the DFT and fast transform. These values affect the numerical integration in time. Also initial values are needed to integrate numerically with respect to time. The time-step size can also influence the accuracy of the numerical integration. Thus, the above-mentioned four factors: 1) grid points, 2) physical plane size, 3) initial values, and 4) time-step size, must be given more discussion from the numerical experiments in the following subsections.

Grid Points

The lines $x = x_i$ and $y = y_j$ are grid lines and their intersections are grid points or mesh points of the grid. When the numerical method is applied to the partial differential equations, the grid lines should be used for the construction of mesh points in computation. With such points, all numerical algorithms are implemented in the entire computational space which is also called the physical plane (x,y plane), as well as the wavenumber plane (k,l plane). These planes are shown in Figure 9.

In principle, the computer code was developed to accommodate any desired value of mesh points in both the x and y directions. However, as will be discussed later, the solution to the equations restricted the number of mesh points used in the algorithm.

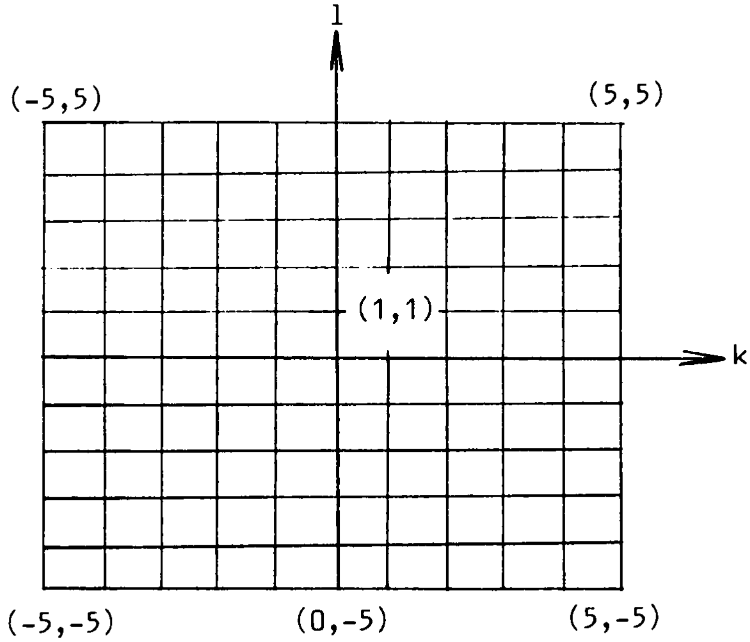

a. Wavenumber Plane

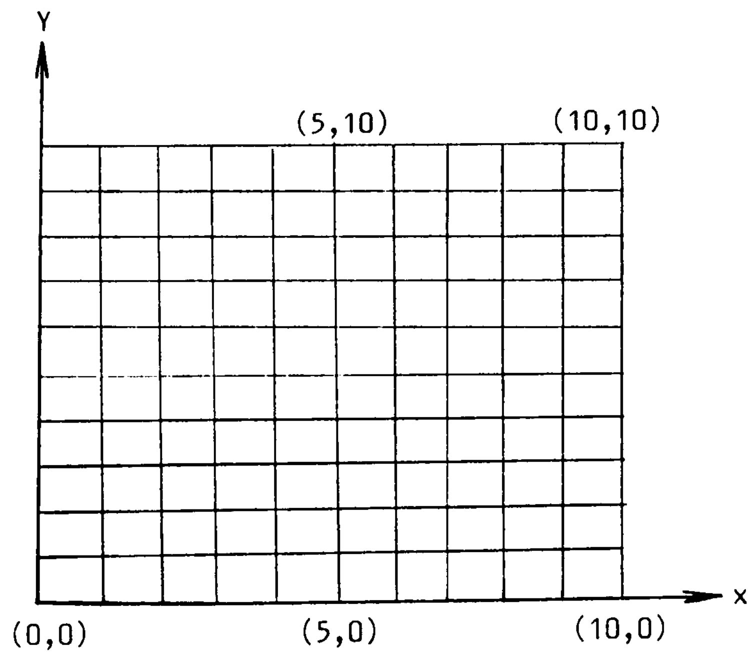

b. Physical Plane

Figure 9. Computation Space.

Initially the simplest example consisting of the 3 x 3 grid points was tried with hand calculation in order to verify the numerical computation. As the results of calculation and computation were coincident, the grid-point numbers were gradually expanded into 5 x 5, 7 x 7,..., 19 x 19 in the numerical tests. In all the tests, the same initial values of A(k,l) and B(k,l), and the same physical plane size are used. In order to determine the optimum grid size for the final use, the code was initially run for only five days with all possible combinations of grid sizes. After examining the variation of the principal mode amplitudes with time, some grid sizes were deemed as nonuseful, while others were useful. Only those grid sizes for which the absolute values of both A(1,1) and B(1,1) were monotonically increasing during the entire five-days computations were deemed to be useful. Below is tabulated all the grid sizes used and the type of results they yielded.

Grid Points	Results
3 x 3	Nonapplicable
5 x 5	Nonapplicable
7 x 7	Applicable
9 x 9	Nonapplicable
11 x 11	Applicable
13 x 13	Applicable
15 x 15	Nonapplicable
17 x 17	Nonapplicable
19 x 19	Nonapplicable

Figure 10 shows the variations of the absolute values of A(1,1) and B(1,1) for two grid sizes of 9 x 9 and 11 x 11 for 14 days. Though their time durations terminate together at 14 days, the patterns of their variation with time are different. The absolute values of A(1,1) and B(1,1) increase monotonically for the 11 x 11 grid points, but not for the 9 x 9 grid points for the first five days because their values decrease. These values are indicated in Table 6. Figure 10 is used only to illustrate the difference between the applicable and nonapplicable cases. Among the above three applicable cases, the grid size of 11 x 11 is the best case due to reasons which will be discussed later. Since the 9 x 9 grid points are not applicable, the 11 x 11 grid points have been chosen for this study. Upon this choice, the computational space in Figure 9 has x_i and y_j for i,j = 0,1,...,10; and wave number k,l = -5,-4,...,4,5.

Physical Plane Size

In the computational space, the different dimensions of this space are used in computing. For the same grid points, 11 x 11, and the same initial values of a(1,1) = 0.015 and B(1,1) = 0.023, varying the sizes of x and y in the physical plane yields the following results:

x or y in km	Results
1000	Nonapplicable
2500	Applicable, shorter time
3140	Applicable, longer time
4500	Nonapplicable
6280	Nonapplicable

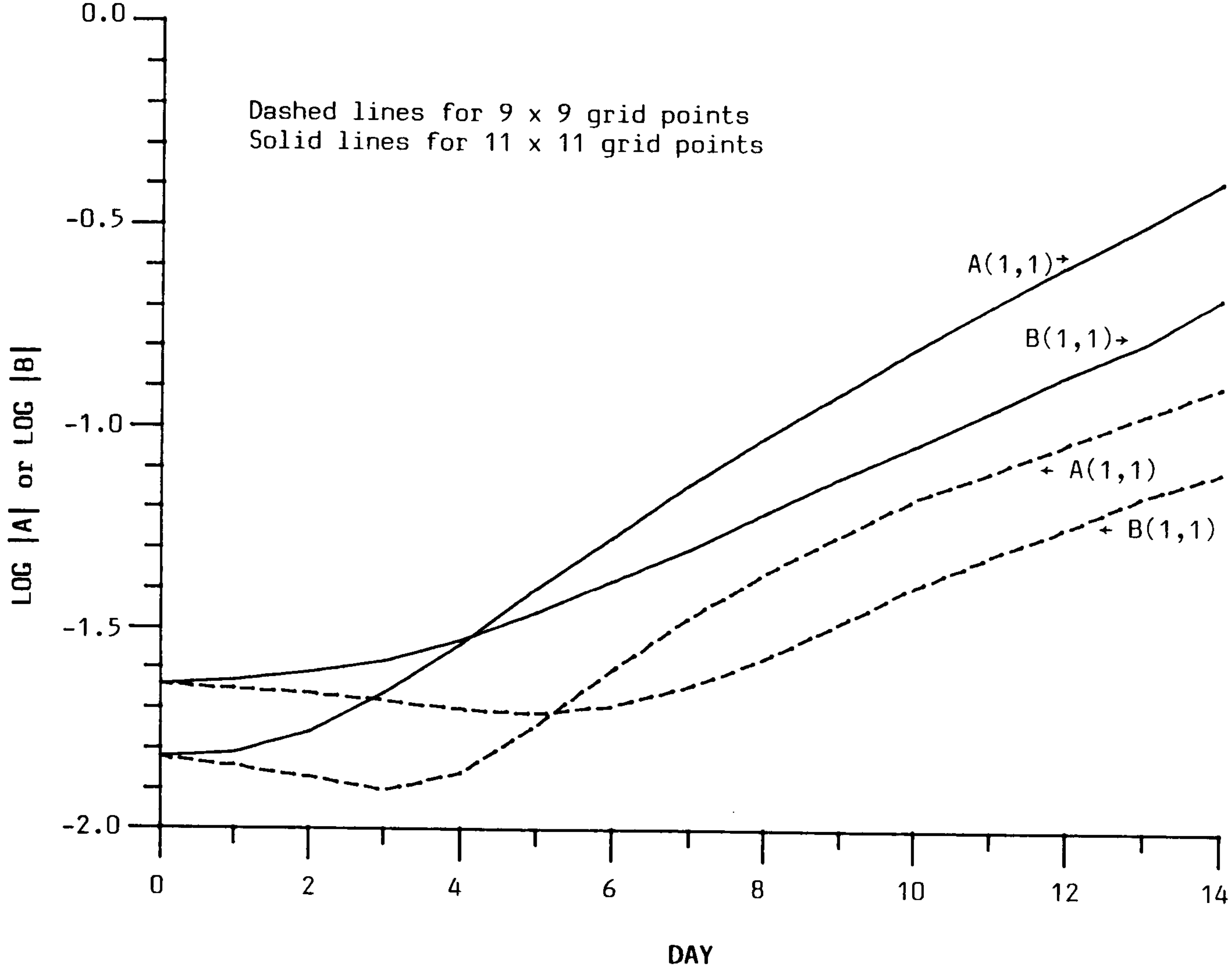

Figure 10. Variation of A(1,1) and B(1,1) with Grid Points.

Table 6. Values of A(1,1) and B(1,1) for 9 x 9 Grid Points.

Items	Results of A(1,1) and B(1,1)					
t(day)	0.00	1.00	2.00	3.00	4.00	5.00
A(1,1)	.0150	.0145	.0135	.0127	.0139	.0182
B(1,1)	.0230	.0227	.0219	.0209	.0198	.0194

Figure 11 shows the results of the numerical integration for the time developments of the principal mode amplitudes A(1,1) and B(1,1) for two different plane sizes of 3140 and 4500 km per side. The tendency of the curves for the 4500 km size indicates that the variations of the absolute values of A(1,1) and B(1,1) do not increase monotonically with time. Table 7 indicates how the absolute values of A(1,1) and B(1,1) decrease in the first 10 days. Therefore, the physical plane size of 4500 km per side is not suitable, but the size of 3140 km is suitable.

Initial Values

From Chapter IV, the equations for the boundary conditions, Equation (4.3), can be reduced to two first-order ordinary equations, Equations (4.23) and (4.24), in time. To solve these simultaneous equations, a set of initial conditions for all mode amplitudes A(k,l) and B(k,l) are needed. Throughout the wavenumber space, there are 121 node points for A and B, respectively, for the mesh size of 11 x 11. The initial values assigned for all points are zero except at point (1,1). Though initial values for A(1,1) and B(1,1) could be chosen arbitrarily, there should be a dependent relationship between them in the numerical tests. This relationship is shown in Table 8.

Table 8 indicates that there are five different ratios of B to A for the physical plane size of 3140 km per side. From the last row of values in Table 8, only the ratio of 1.5 appears to be better than the others for the larger duration. No matter what ratio is

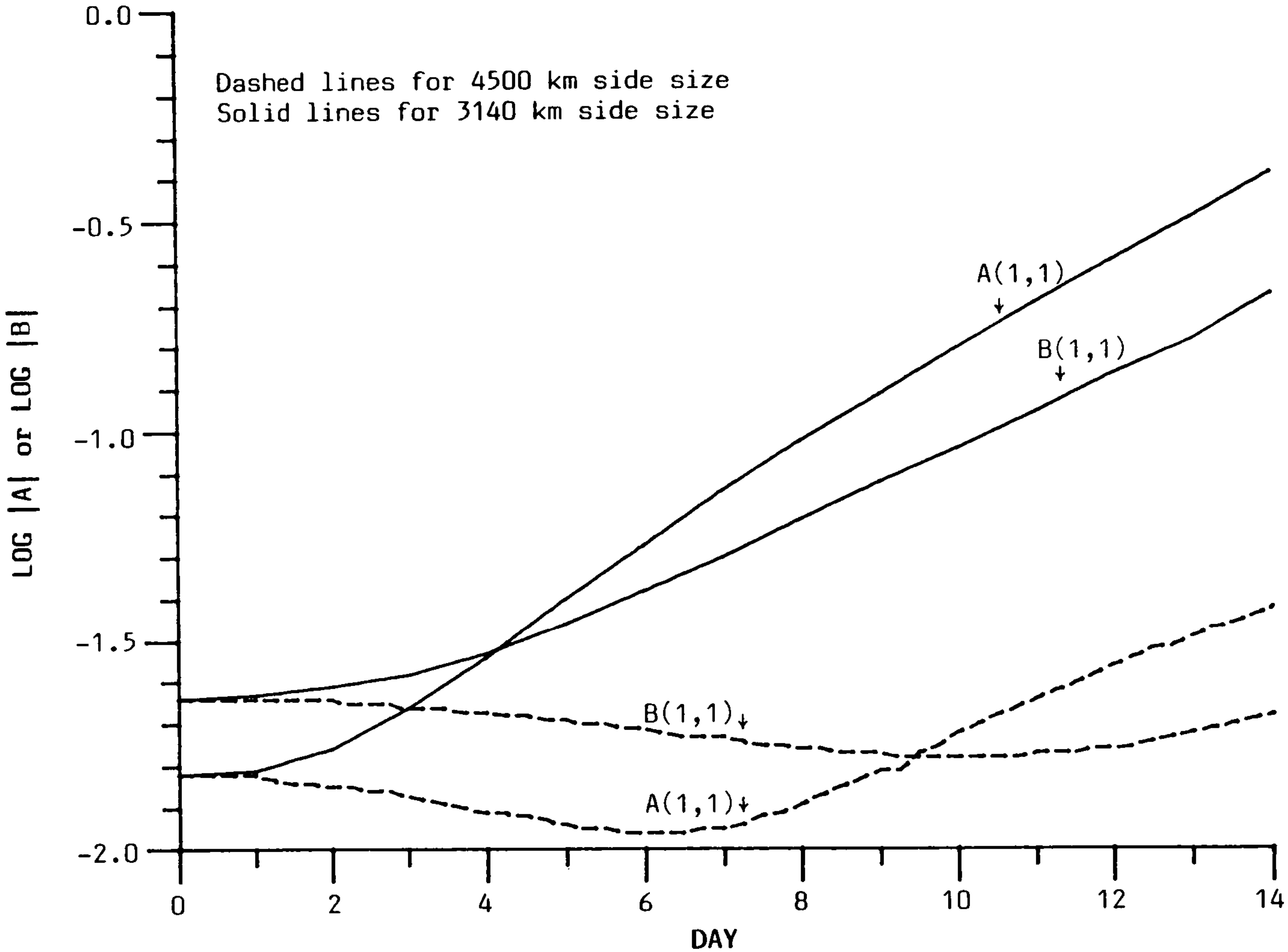

Figure 11. Variation of A(1,1) and B(1,1) with Physical Plane Size.

Table 7. Values of A(1,1) and B(1,1) for x = y = 4500 km.

Items	Results of A(1,1) and B(1,1)					
t(day)	0.00	2.00	4.00	6.00	8.00	10.00
A(1,1)	.0150	.0143	.0124	.0110	.0128	.0189
B(1,1)	.0230	.0225	.0218	.0194	.0175	.0165

Table 8. Initial Values for B/A.

Items	Results for B/A Varied					
A(1,1)	0.15	0.20	0.20	0.15	0.40	0.50
B(1,1)	0.45	0.40	0.30	0.23	0.40	0.40
B/A	3.00	2.00	1.50	1.50	1.00	0.80
t(day)	4.00	4.00	5.00	5.00	4.00	4.00

used, the variation with time for A(1,1) always grows more rapidly than that for B(1,1).

In a number of numerical experiments, the initial values for the principal mode amplitudes A(1,1) and B(1,1) are varied; but the grid size is fixed to 11 x 11, and the side size of the physical plane is also fixed to 3140 km. The test results are tabulated in Tables 9 and 10, and shown in Figures 12, 13, and 14, respectively.

Comparing the results in Tables 9 and 10, it appears that the smaller the initial value becomes, the longer the time endures. The too small initial values mean that the initial pressure perturbation is too weak to induce the early growth of the higher harmonic waves, which is an undesirable condition in this study. For compromise, the initial values for A(1,1) = 0.015 and B(1,1) = 0.023 are used hereafter in the computation. The last rows of the tables denote the final time in days. Beyond each final time, blow-up of the integration occurs.

Figures 12 and 13 indicate that the time developments for A(1,1) or B(1,1) terminate at 8, 9, 10, 11 and 14 days, respectively, due to the different initial values. All the lines have different terminations, but they are nearly parallel. Beyond each terminal, the integration has blow-up. Figure 14, being slightly different from Figures 12 and 13, exhibits the time evolution of A(1,1) and B(1,1) through five days' duration for initial values of A(1,1) = 0.15 and B(1,1) = 0.23, and 14 days' duration for A(1,1) = 0.015 and B(1,1) = 0.023. This figure also exhibits that the initial values of a different order of magnitude make nine days' difference in

Table 9. Initial Values for Shorter Time.

Items	Results for B/A = 1.5					
A(1,1)	0.60	0.50	0.40	0.30	0.20	0.15
B(1,1)	0.90	0.75	0.60	0.45	0.30	0.23
t(day)	2.00	2.00	3.00	3.00	5.00	5.00

Table 10. Initial Values for Longer Time.

Items	Results for B/A = 1.5					
A(1,1)	0.060	0.050	0.040	0.030	0.020	0.015
B(1,1)	0.090	0.075	0.060	0.045	0.030	0.023
t(day)	8.00	9.00	10.00	11.00	11.00	14.00

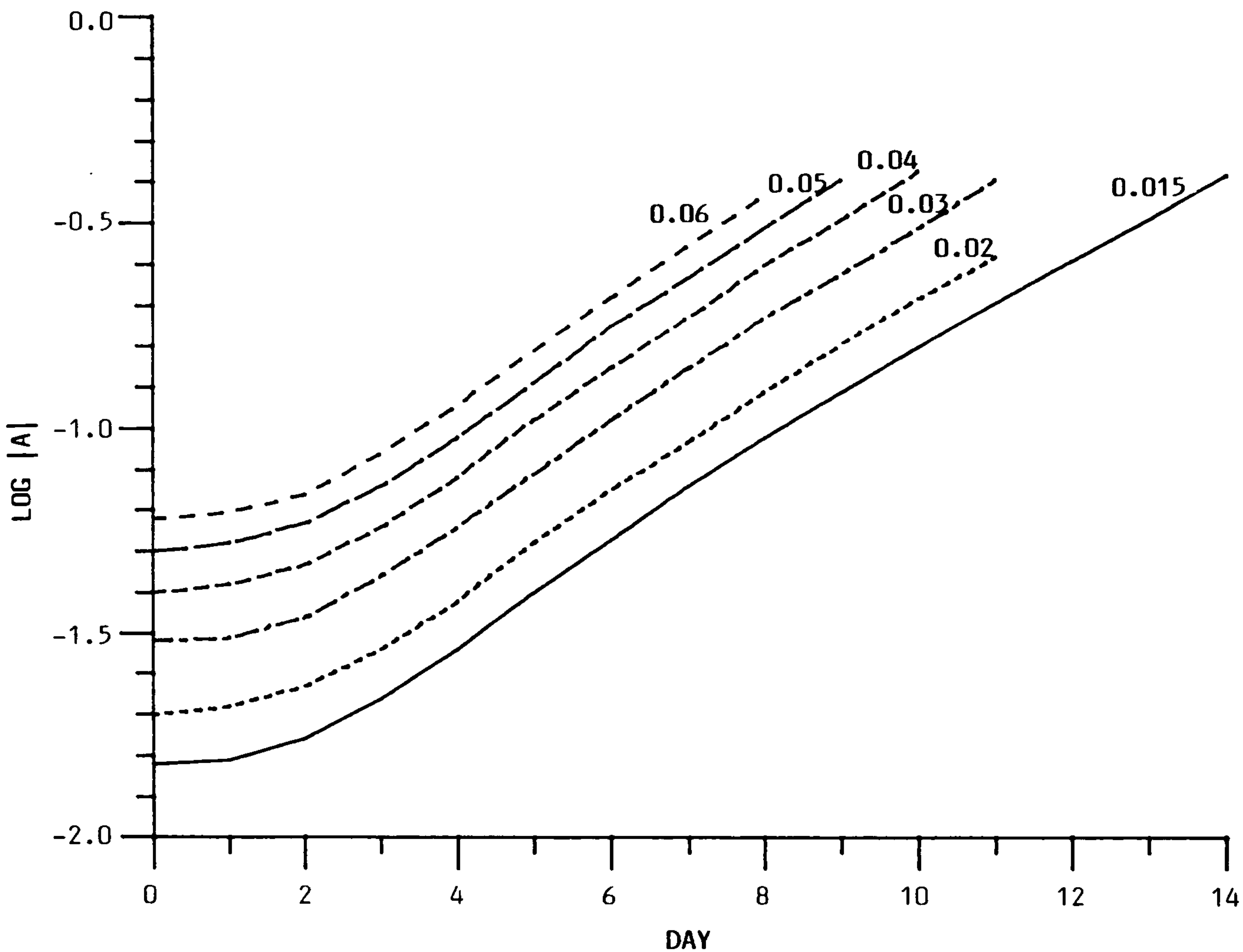

Figure 12. Variation of A(1,1) with Initial Values.

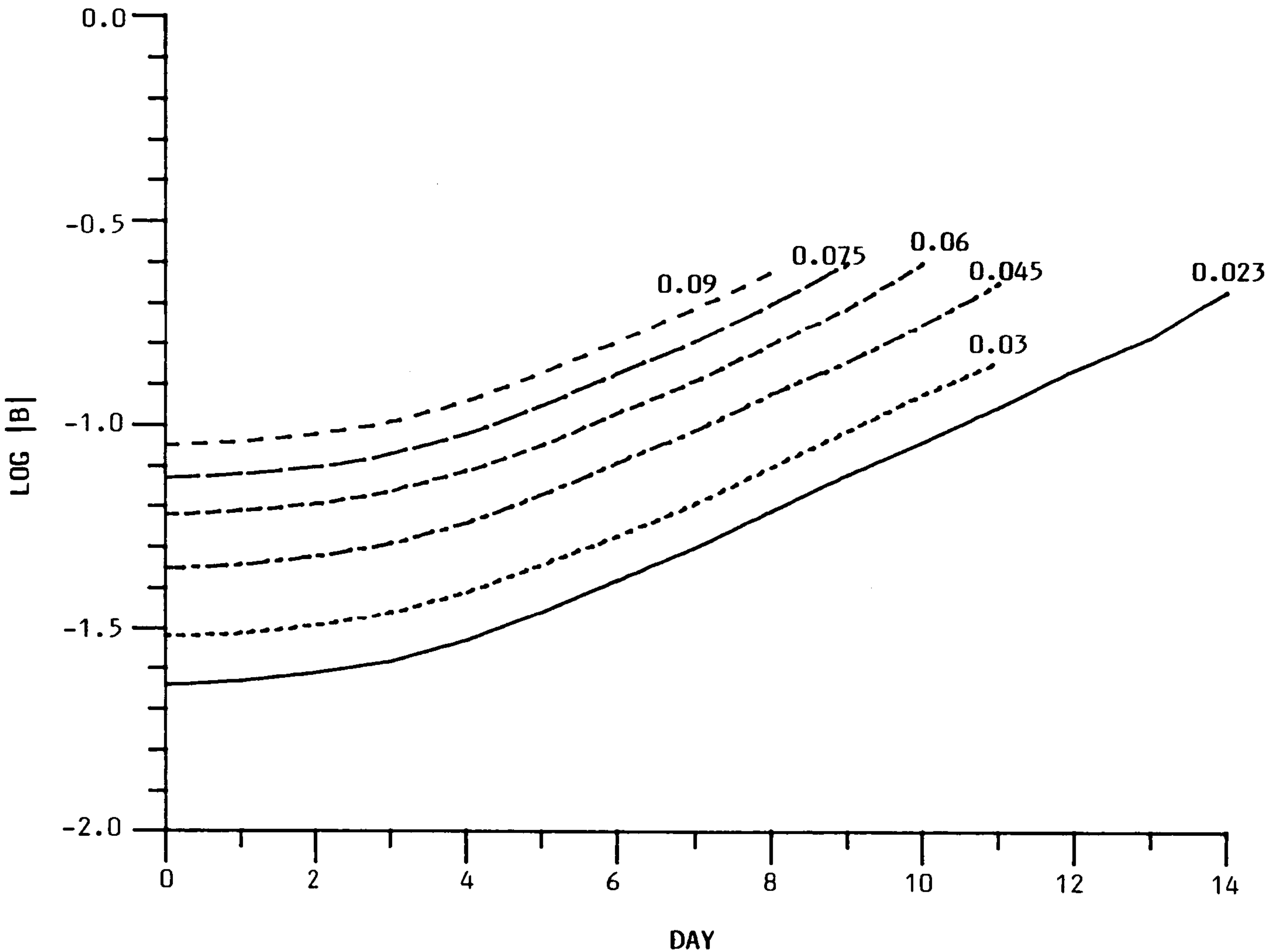

Figure 13. Variation of B(1,1) with Initial Values.

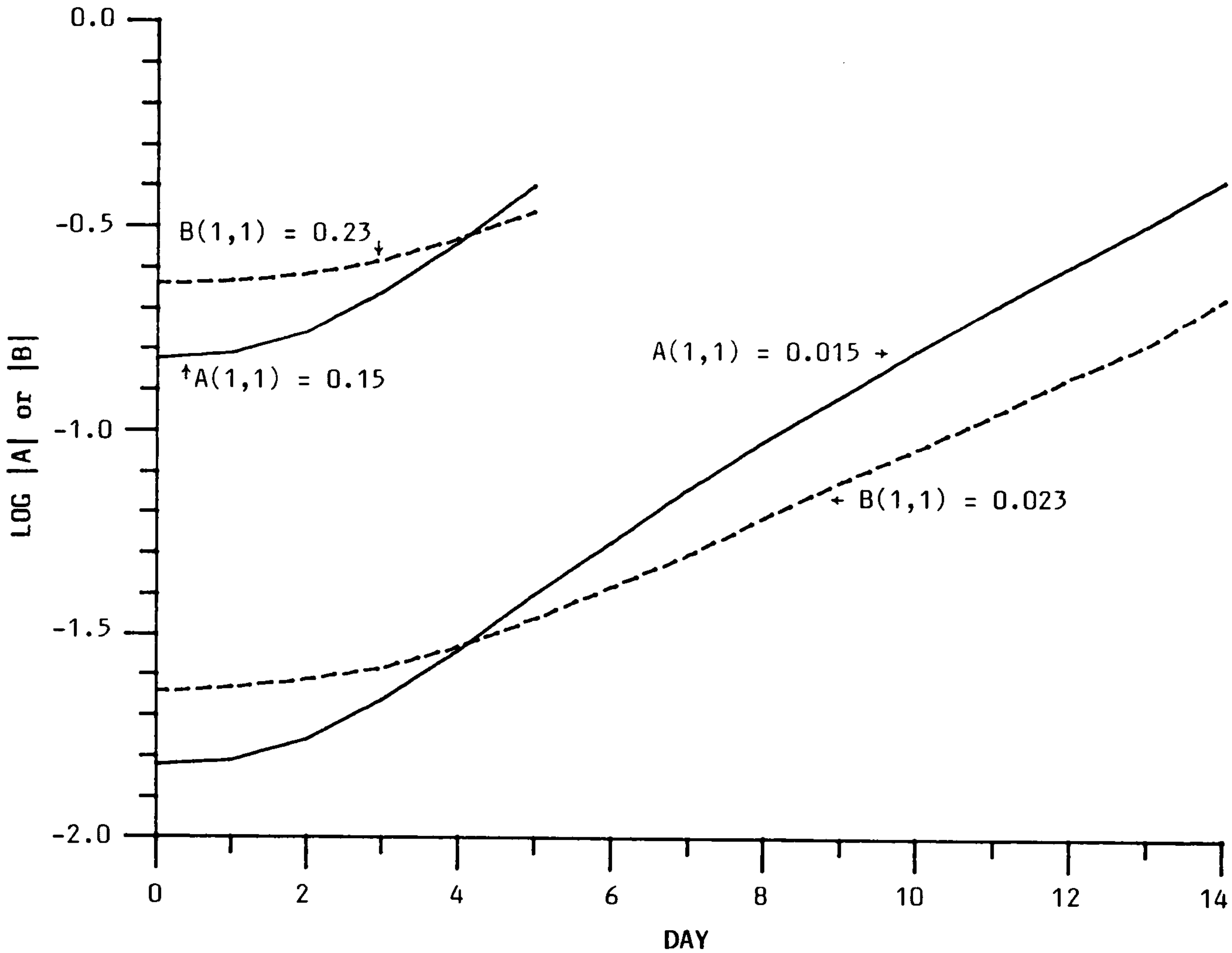

Figure 14. Variation of A(1,1) and B(1,1) with Initial Values.

time duration. From the point of view of time duration, the longer, the better; so the final time of 14 days is desirable. In Figure 14, blow-up also occurs beyond each time limit.

Time-Step Size

In Equations (4.23) and (4.24) of Chapter IV, the continuous approximations to the solutions of $A(k,l,t)$ and $B(k,l,t)$ are not sought; instead, approximations to A and B are generated at mesh points in a finite time interval. From initial time to final time, a series of steps are used to find these numerical approximations. The common distance between each time step is the time-step size. In the principle of numerical analysis, the small step size produces more steps in time interval and makes the results more accurate. Several different step sizes were used in the numerical integration from initial time to final time (14 days). The obtained results are listed in Table 11. The first column denotes five different step sizes; the second one shows the number of steps needed in time interval (or 14 days); the third and fourth ones exhibit the absolute values of $A(1,1)$ and $B(1,1)$ at the final time.

In Table 11, the absolute values of $A(1,1)$ and $B(1,1)$ change a little when the step size changes from 0.1 to 0.05. Therefore, the time-step size does not alter the results considerably and is fixed to $\Delta t = 0.05$ because of the restriction of the use of the computer time. Also, $\Delta t = 0.05$ is satisfied with the condition $\Delta t \leq 8/11^2$ given in Equation (3.10) of Chapter III. Here the time-step size $\Delta t = 0.05$ is equivalent in dimensional quantity to $\Delta t^* = 1/2$ hour.

Table 11. Relationship Between Δt and A(1,1), B(1,1).

Δt	Steps	A(1,1)	B(1,1)
0.05	708	.413824	.212336
0.10	364	.410392	.204819
0.20	192	.396698	.196842
0.40	105	.377106	.188507
0.80	062	.345915	.176530

Results

The numerical investigation is aimed at finding all the coefficients A(k,l) and B(k,l) in time for the use in the perturbation stream function $\phi(x,y,z,t)$. Then the configuration of this stream function represents various wave patterns which are treated in the following subtopics.

Time Evolution of A(k,l) and B(k,l)

The previous section concentrated on the discussion of the time evolution of the principal mode amplitudes A(1,1) and B(1,1). Owing to the complex conjugate relationships given in Equations (4.9) through (4.12), the initial values for modes A(-1,-1) and B(-1,-1) are the same as that for modes A(1,1) and B(1,1); the time developments of A(-1,-1) and B(-1,-1) are also the same as that of A(1,1) and B(1,1), respectively. During the numerical integration in time, the values of the wave amplitudes A(k,l) and B(k,l) seem to have no variation in the first nine days except for A(1,1) and B(1,1). After nine days, a few higher harmonic waves appear in a substantial way. These phenomena are shown in Figure 15 for A(k,l) and Figure 16 for B(k,l). Figures 15 and 16 also show that the slopes of the time-development curves for the higher harmonic modes are steeper than that for the principal modes. A few higher harmonic modes appear at a later time, but blow-up occurs with the principal modes immediately after the final time of 14 days.

From Figures 10 through 16, there appear two main features of the time evolution of A(k,l) and B(k,l) in the computational space. The

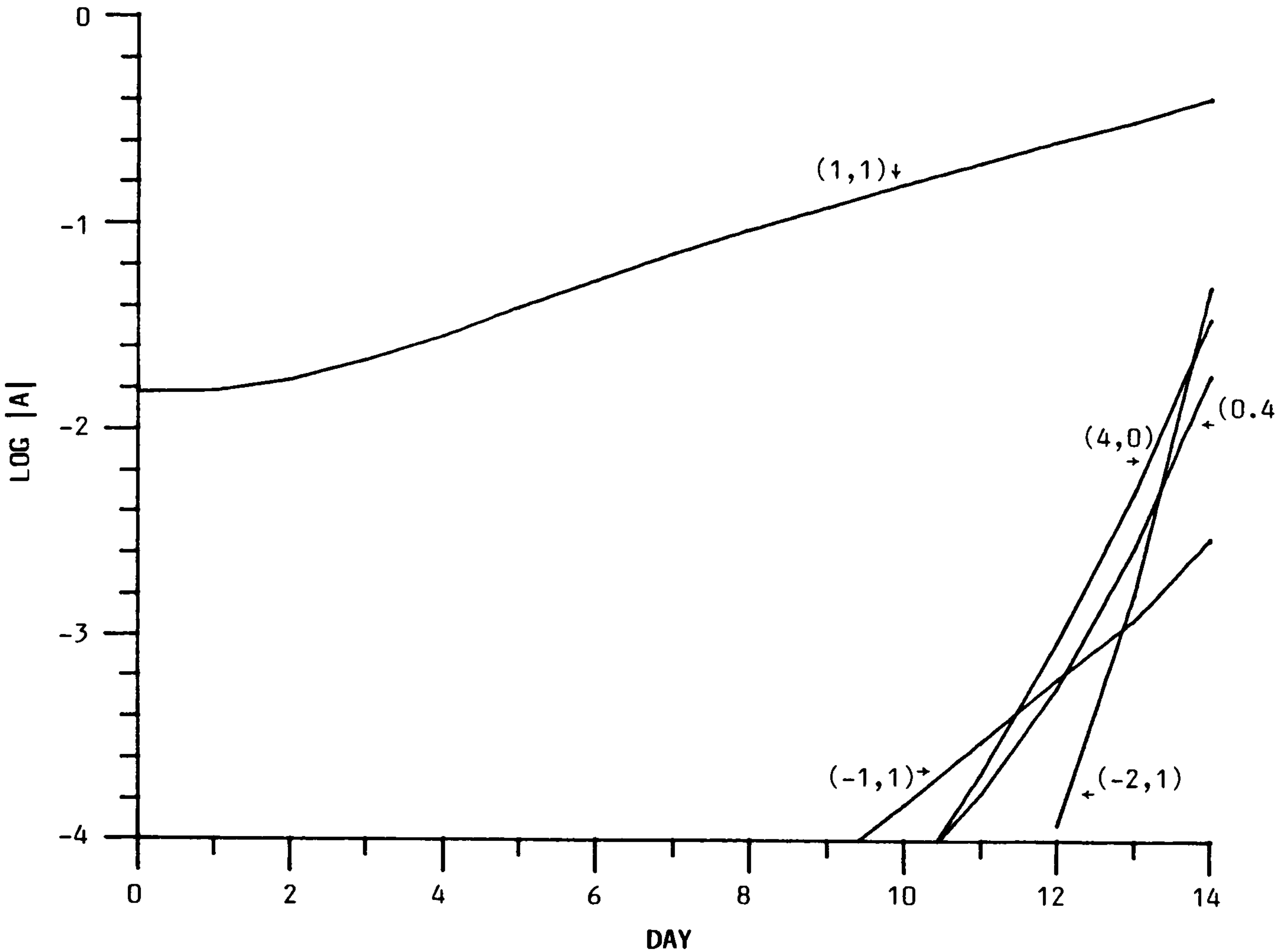

Figure 15. Time Evolution of A(k,l).

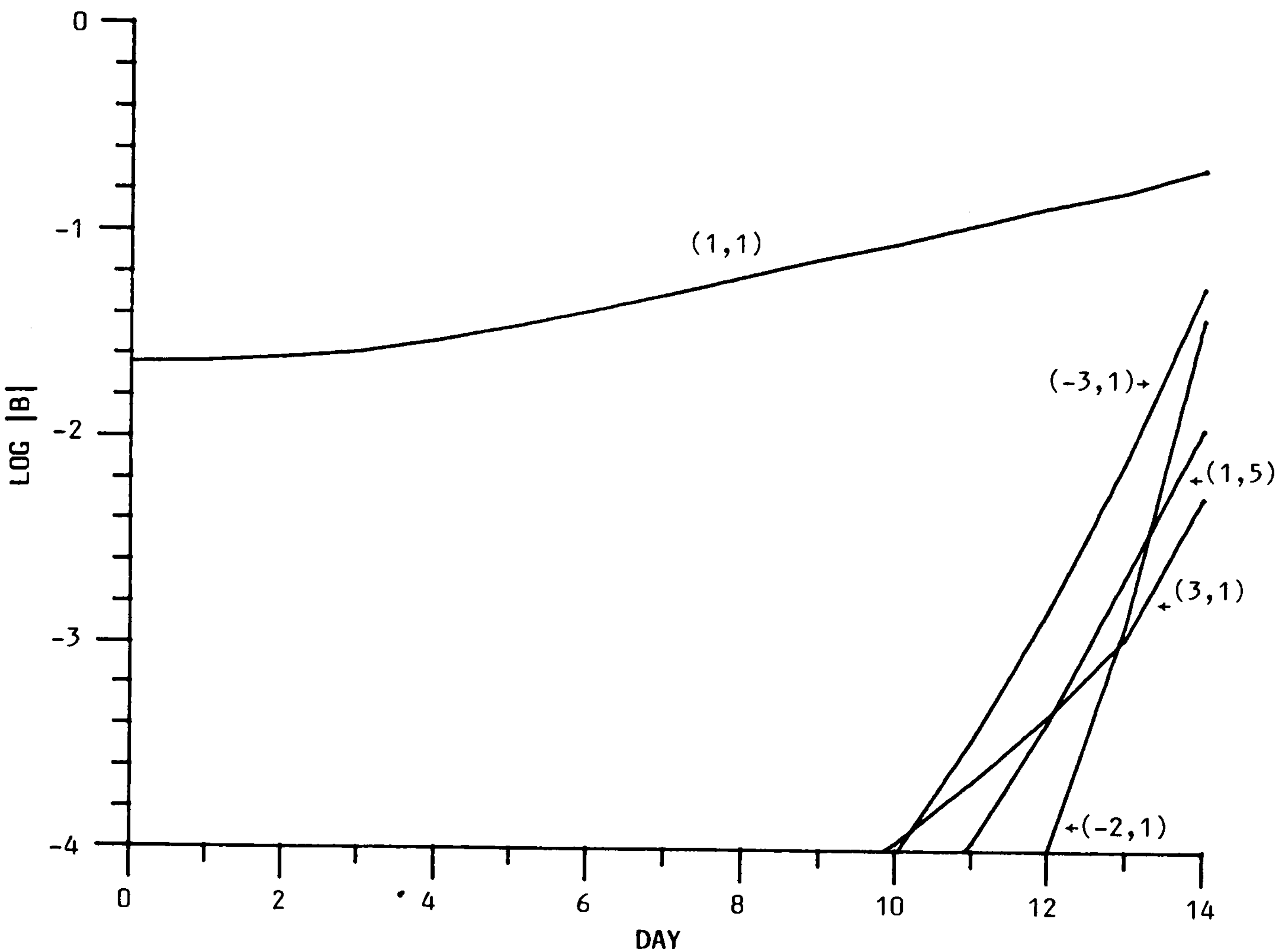

Figure 16. Time Evolution of B(k,1).

first one is concerned with factors of the grid points, the physical plane size, and initial values. The optimum time evolution for these wave amplitudes A(k,l) and B(k,l) depends upon the optimization of these three factors.

The second feature is the problem of blow-up. In our numerical investigations, all the applicable time-development curves have their own time terminations. Beyond these different time limits, they are confronted with the same problem of blow-up at a specific time. For example, the values of A(1,1) and B(1,1) increase from 0.015 and 0.023 at the initial time to 0.673 and 0.527 (absolute values hereafter) at $14\frac{1}{2}$ days, respectively. For two more time steps, they reach the values of 1.507 and 0.670, respectively. For one more time step again, they suddenly change into 9.828 and 5.805. At $14\frac{3}{4}$ days, they have the same result--blow-up. This sudden change occurs at a special condition which corresponds to the critical condition of the Eady linear problem. In Chapter II, the quadratic equation, Equation (2.89), from the boundary condition of the Eady problem was shown to have a critical value of $\mu_c = 2.3994$. If one root of this equation is less than μ_c, the baroclinic instability possibly exists in the Eady problem. In our nonlinear problem, as this critical value is approached, all the time-development values for the absolute A(k,l) and B(k,l) change abruptly, and ultimately blow up. The possibility of this phenomenon comes from the instability of the Eady linear problem. It is also possible that the atmospheric turbulence could grow at the expense of the energy in waves by wave-breaking phenomena after 14 days. Owning to the growth of the turbulence, blow-up may occur.

Wave Patterns

Plane Waves. In Chapter IV, there are three equations, (4.41), (4.42), and (4.43), for different height levels. They are used here to compute the numerical values for plotting the curves shown in Figures 17 through 20 in the following two cases:

Case 1 corresponds to the initial time. The initial perturbation waves are cosine curves with different amplitudes for three height levels. Figure 17 illustrates these waves propagating along the x direction, but y and z are fixed at $y^* = 785$ km and $z^* = 5$ km, and at $y^* = 942$ km and $z^* = 10$ km, respectively. At ground level, the wave amplitude is so small that the wave shape almost becomes a straight line.

Case 2 corresponds to the final time, 14 days. From initial to final time, the numerical tests exhibited the small variation in the perturbed waves at $t^* = 7$ days and $t^* = 10$ days, respectively, because modes $A(k,l)$ and $B(k,l)$ have response only after nine days. So the results from these tests are neglected. Figures 18 through 20 indicate the results obtained at the final time.

Figure 18 exhibits two waves at ground level. They propagate along the x direction with nearly the same amplitudes. The solid line is for $y^* = 2512$ km, while the dashed one is for $y^* = 2747$ km. Both of them are similar to the steady waves in the rotating annulus experiment. Figure 19 shows two waves at mid-height ($z^* = 5$ km) level. Their amplitudes are so small that the waves seem to be negligible. Figure 20 indicates the unstable waves at upper level ($z^* = 10$ km) and at $y^* = 628$ km (solid) and at $y^* = 785$ km (dashed), respectively.

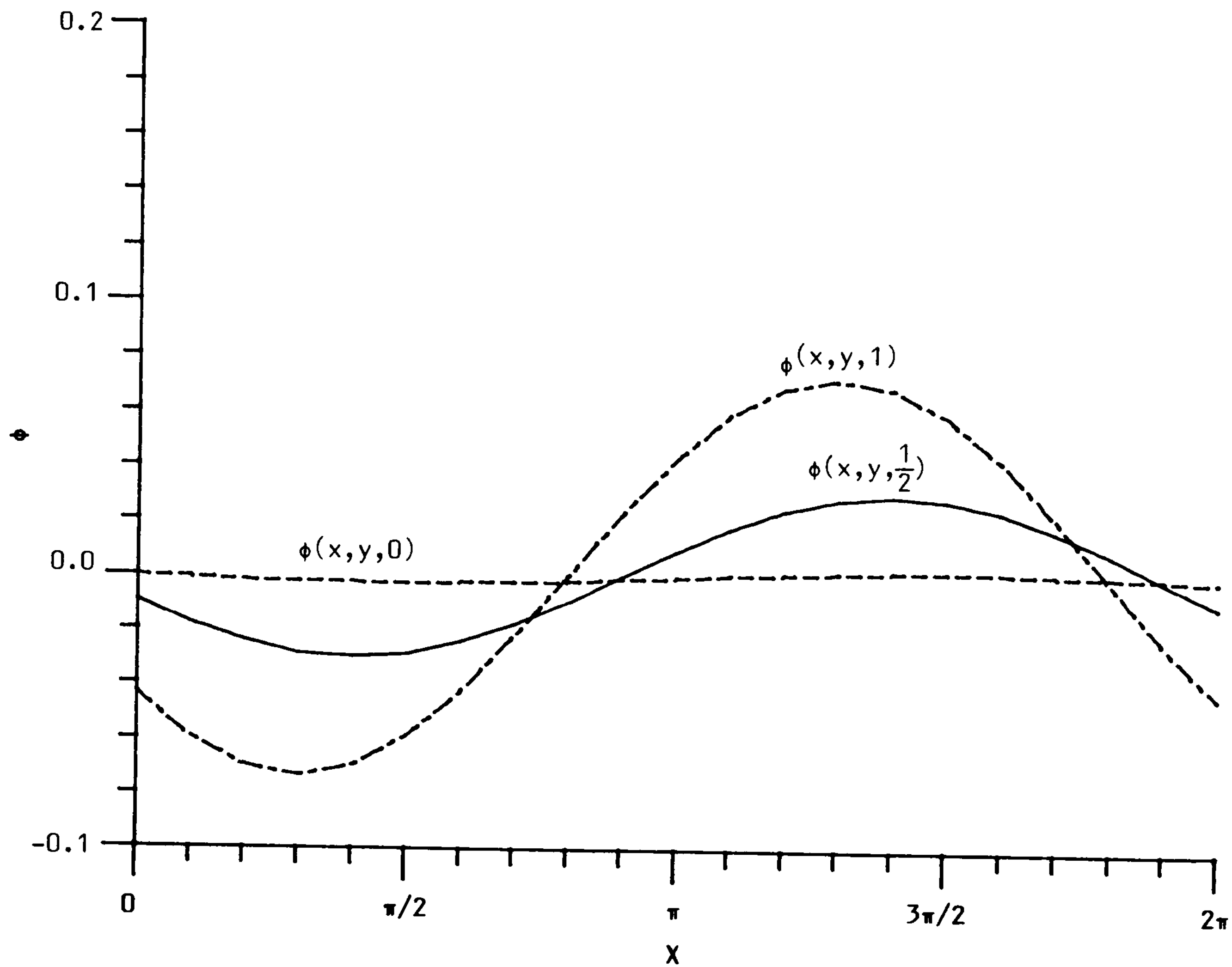

Figure 17. Plane Wave for $\phi(x,y,z)$ at $t^* = 0$.

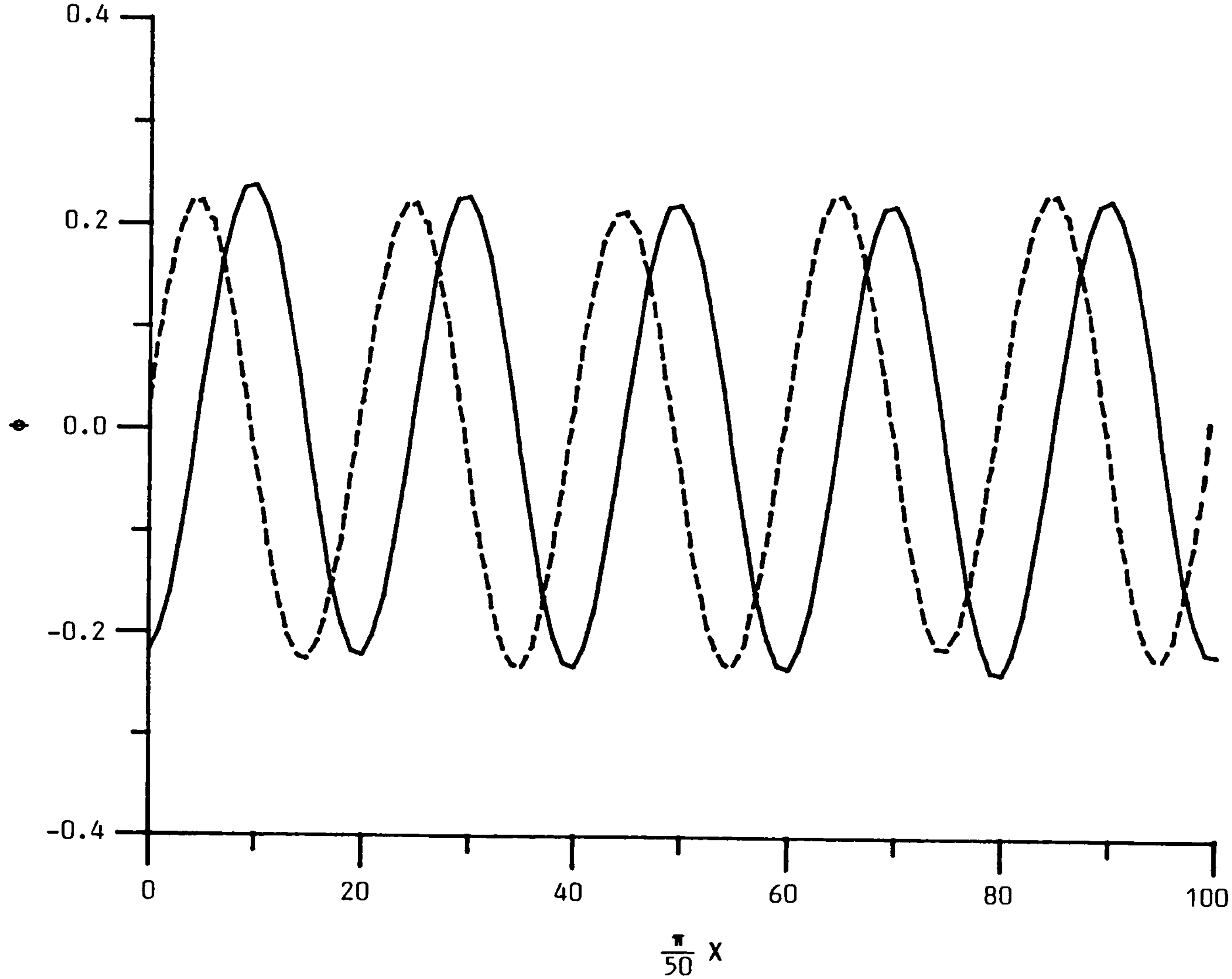

Figure 18. Plane Wave for $\phi(x,y,0)$ at t^* = 14 Days.

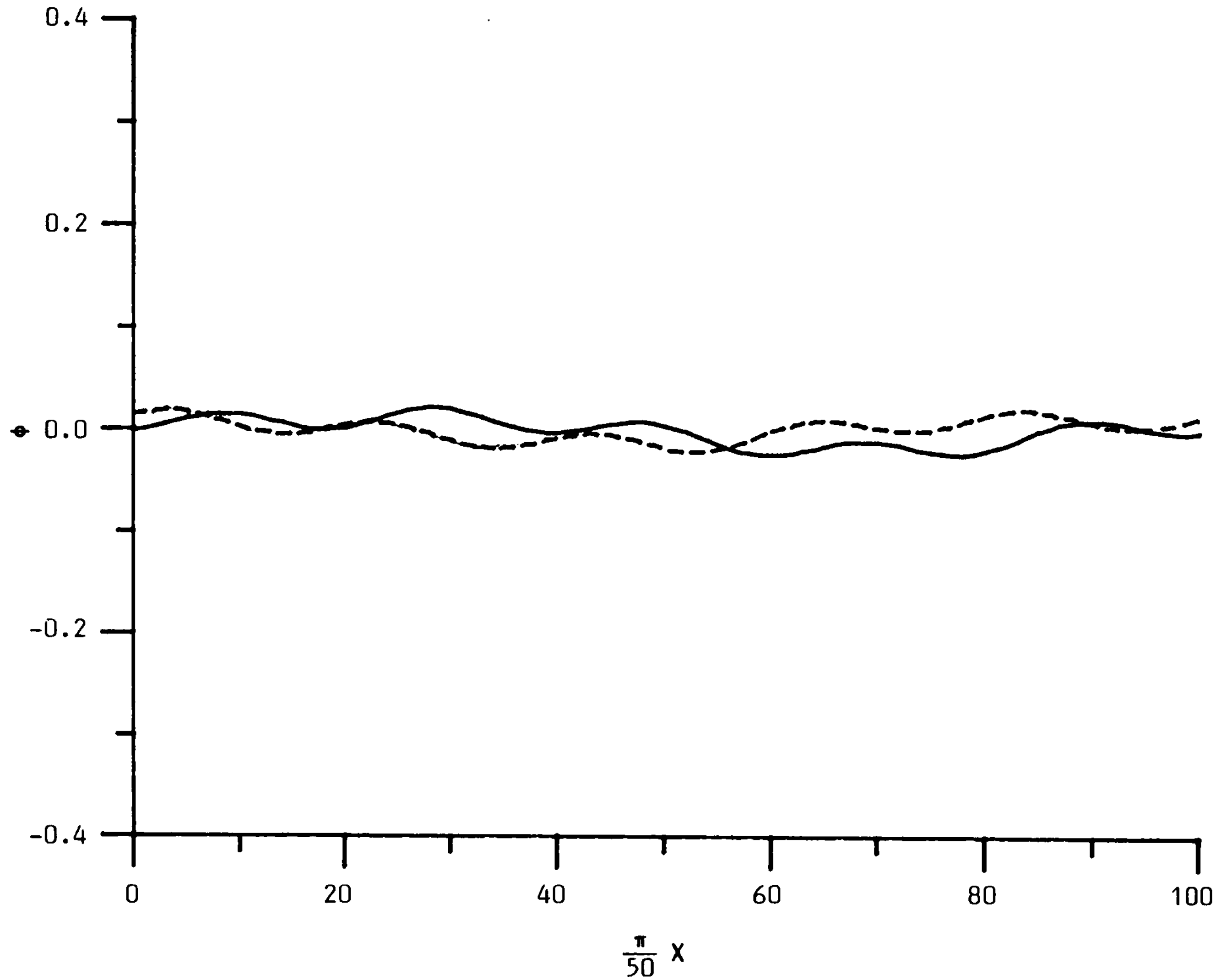

Figure 19. Plane Wave for $\phi(x,y,\frac{1}{2})$ at t* = 14 Days.

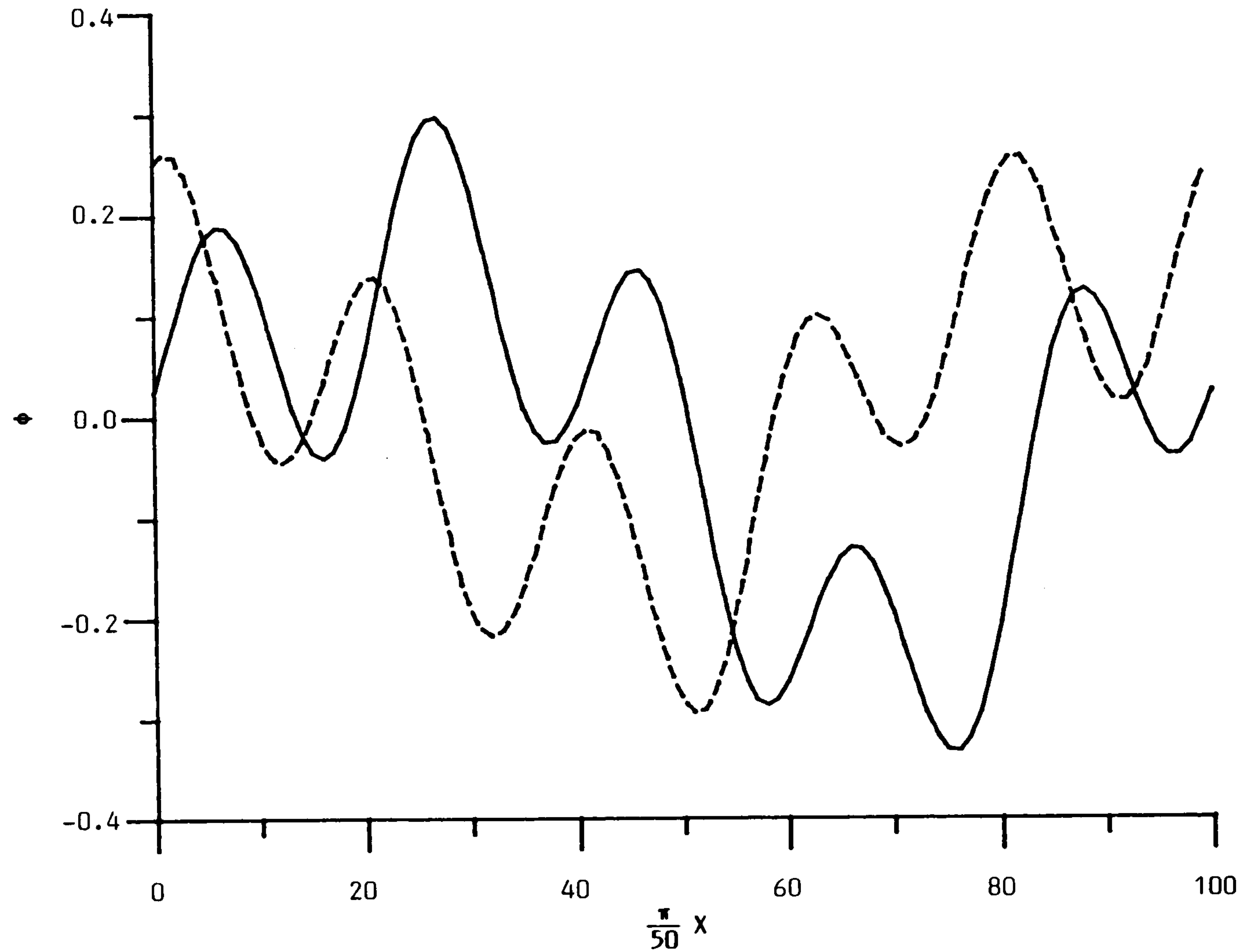

Figure 20. Plane Wave for $\phi(x,y,1)$ at $t^* = 14$ Days.

Contour Plotting. In Chapter II, Equations (2.53) and (2.54) indicate that pressure can serve as stream function. However, in the nonlinear problem, the perturbation stream function serves as perturbation pressure. The locus of points of equal pressure are used in topographic mapping. Contour lines or curves represent a uniform series of pressure, and the difference in pressure between adjacent lines or curves is the contour interval of the given map. Thus, contours represent the shape of the undulation of the flow field on the flat map surface; but, generally, they do not cross each other in the plotting.

Using The University of Tennessee Space Institute (UTSI)/National Center for Atmospheric Research (NCAR) package, the contour plottings for $\phi(x,y,z)$ at different times are shown in Figures 21 through 25. At initial time, owing to the very small wave amplitudes shown in Figure 17, contours for $\phi(x,y,0)$, $\phi(x,y,\frac{1}{2})$, and $\phi(x,y,1)$ are featured with a few straight, tilted dividing lines (labeled with 0.0) similar to that shown in Figure 21. So these contours at $t = 0$ are omitted here. At 10 days, contours are represented in Figures 21 and 22. The contour for ground level has only a few dividing lines and is also omitted. Figure 21, for mid-height level, exhibits several straight, tilted dividing lines with absence of contours; and Figure 22, for the upper level, indicates contour lines parallel to the dividing ones.

At final time, 14 days, the situation is changed. Figure 23 shows the contour lines at ground level. Some lines (labeled with 0.02) lie in a high-pressure and some (labeled with -0.02) lie in a

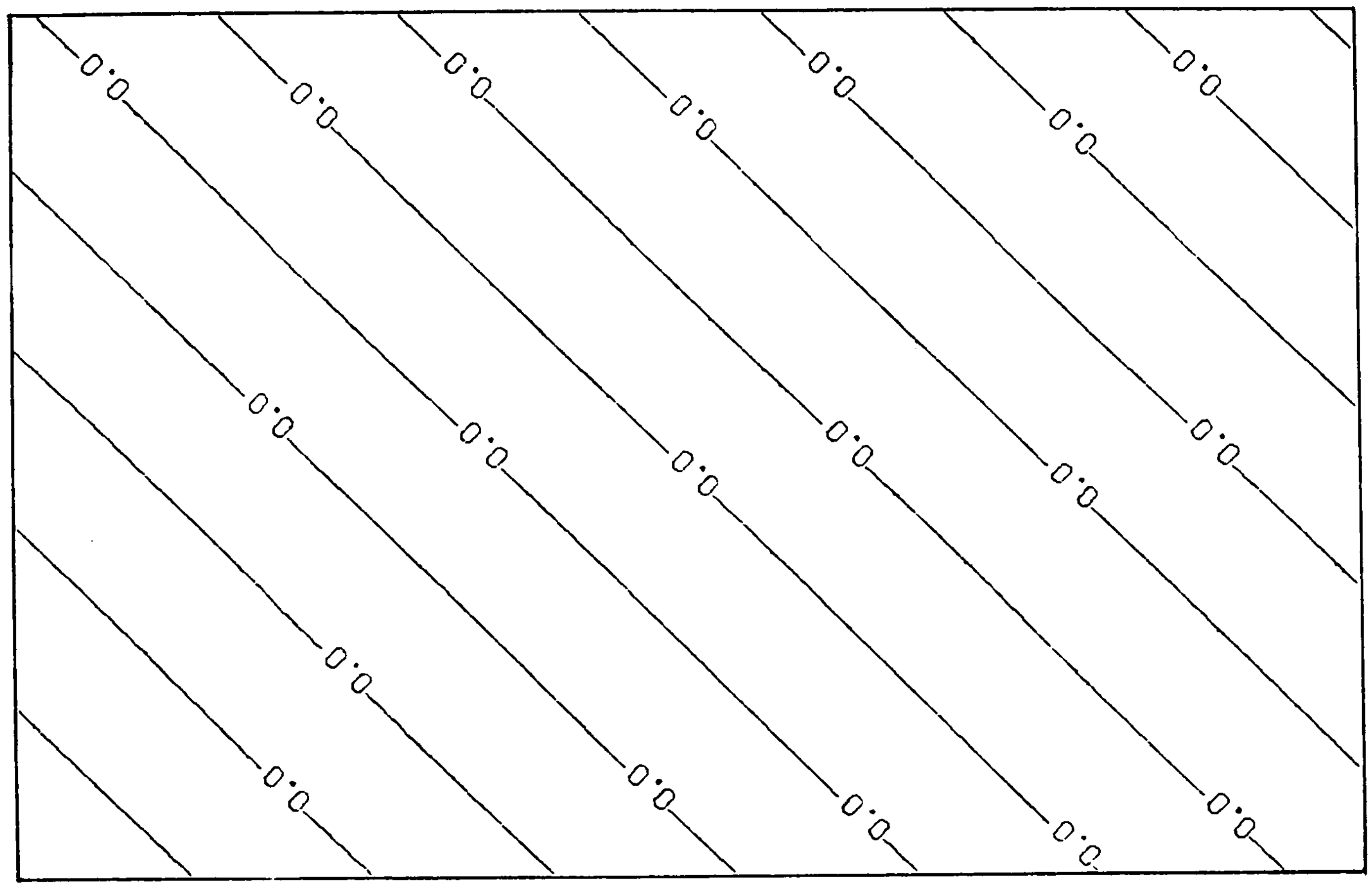

Figure 21. Contour of $\phi(x,y,\frac{1}{2})$ at $t^* = 10$ Days.

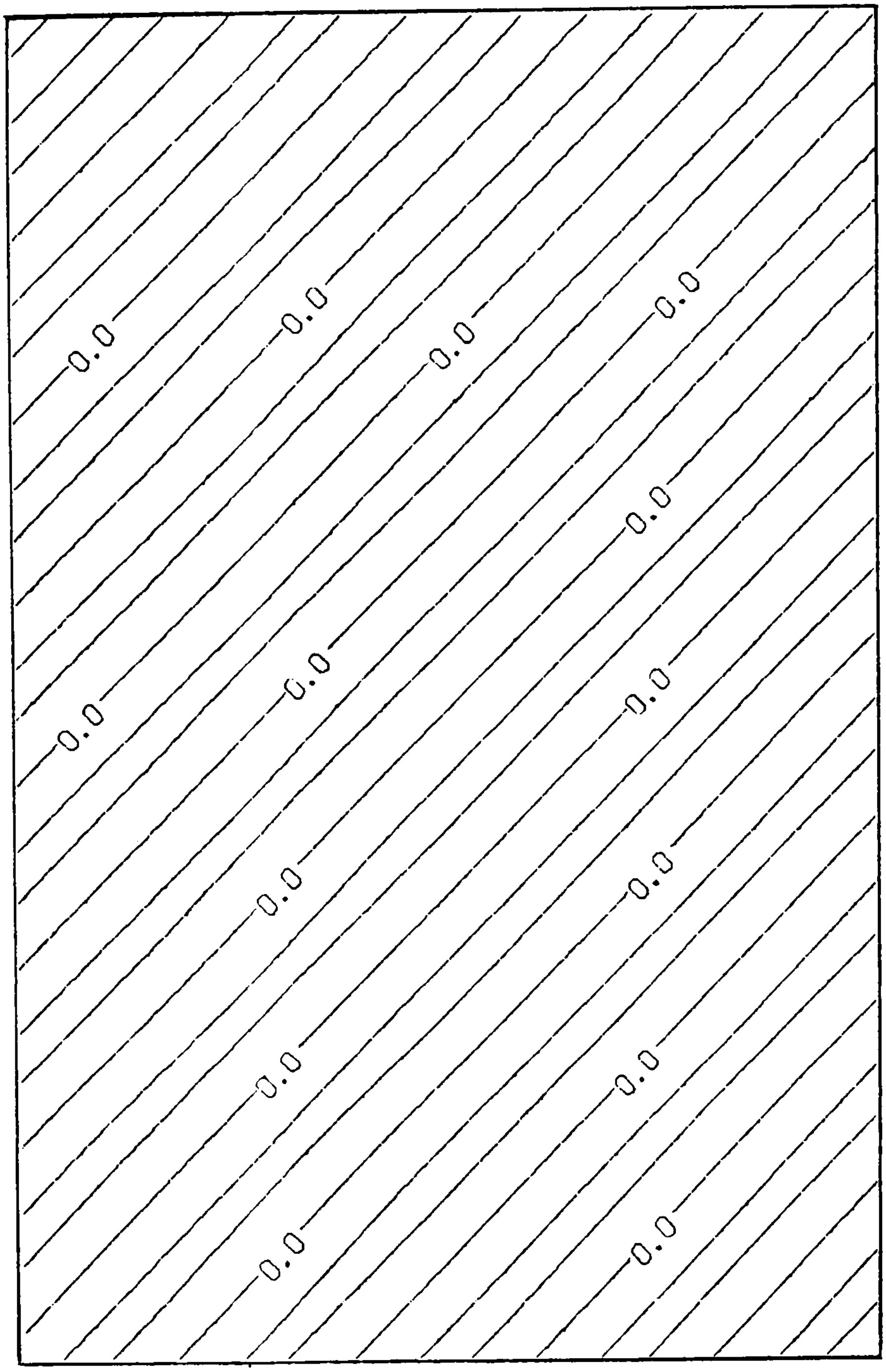

Figure 22. Contour of $\phi(x,y,1)$ at $t^* = 10$ Days.

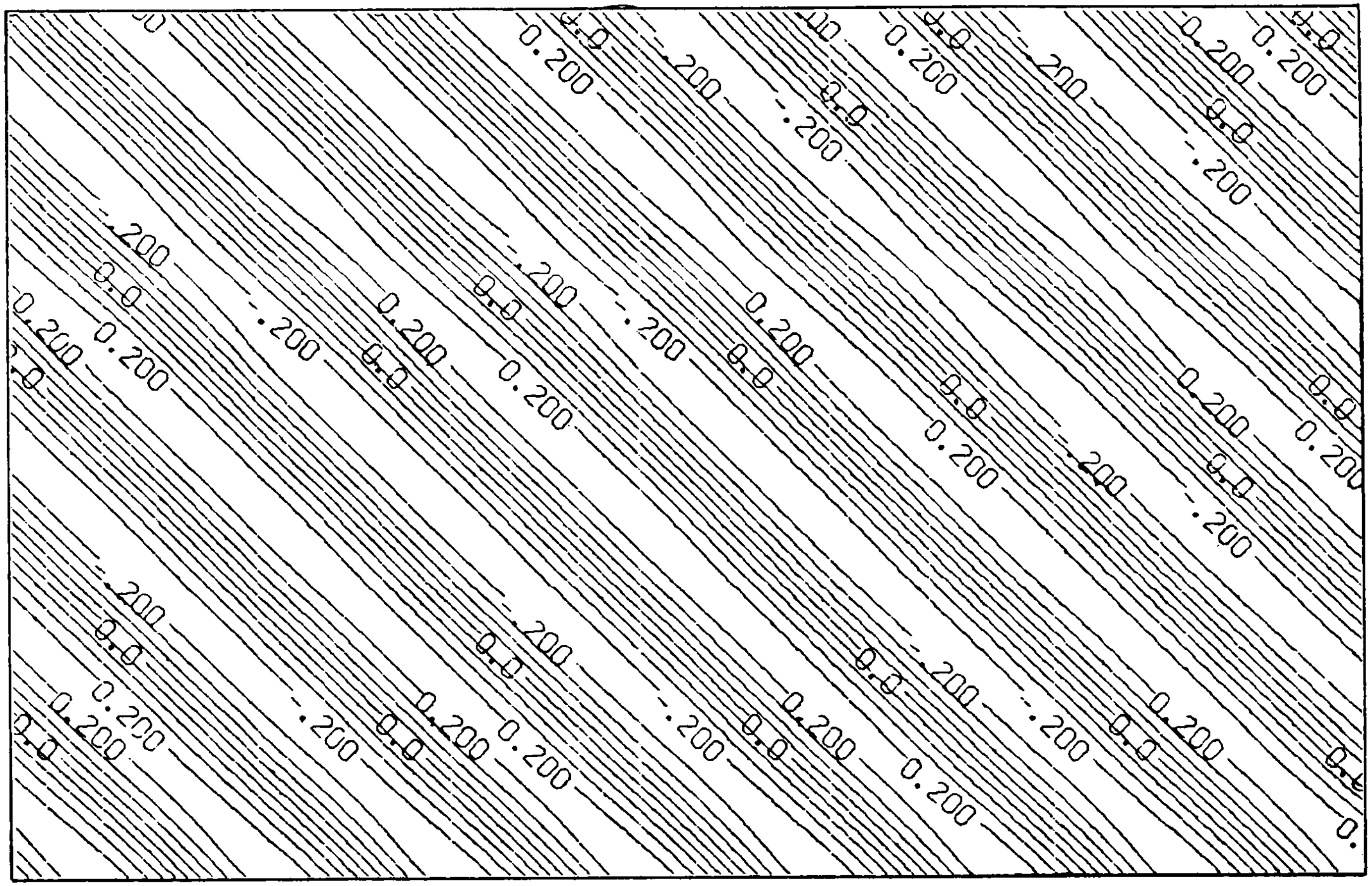

Figure 23. Contour of $\phi(x,y,0)$ at $t^* = 14$ Days.

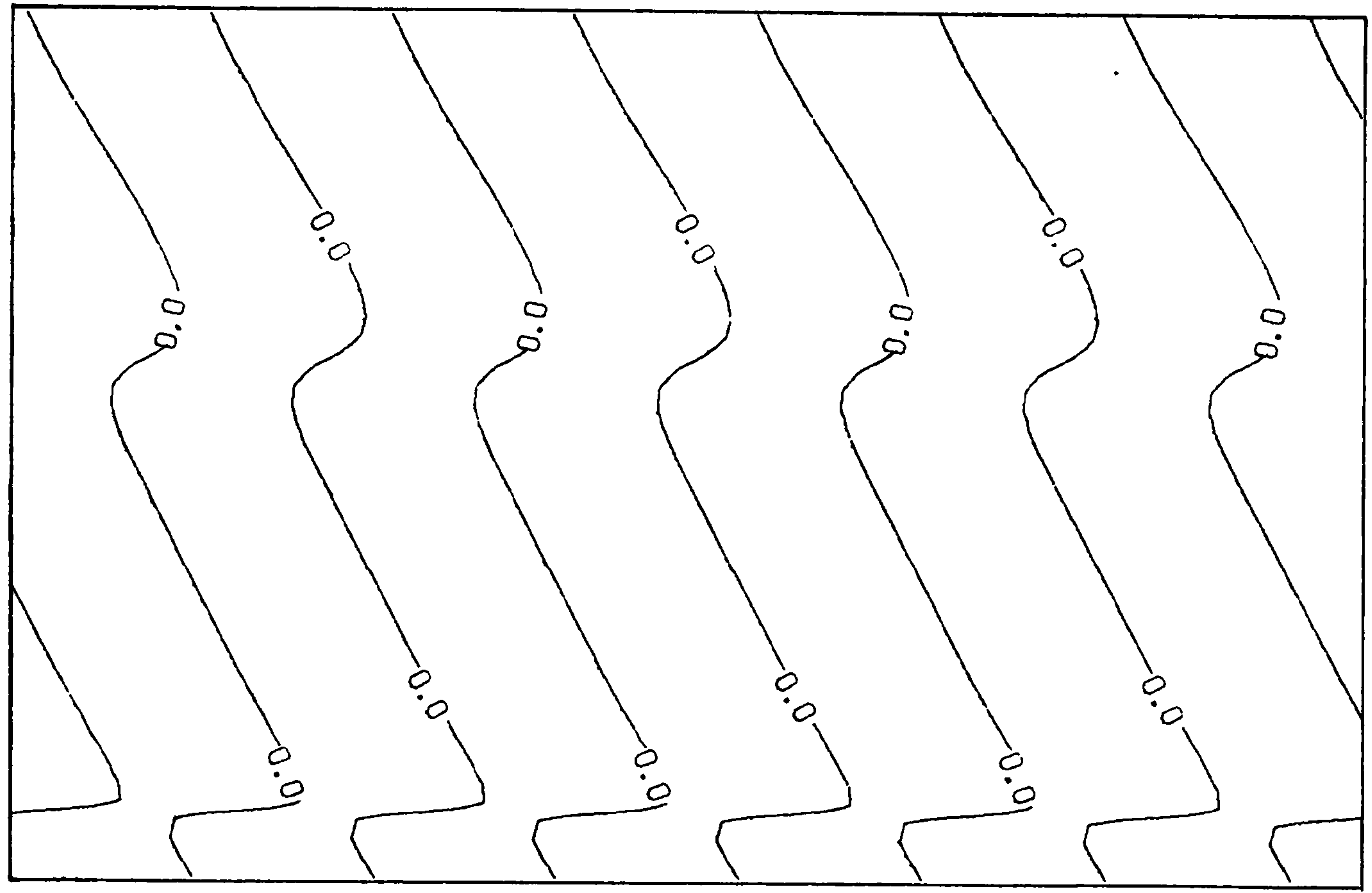

Figure 24. Contour of $\phi(x,y,\frac{1}{2})$ at t^* = 14 Days.

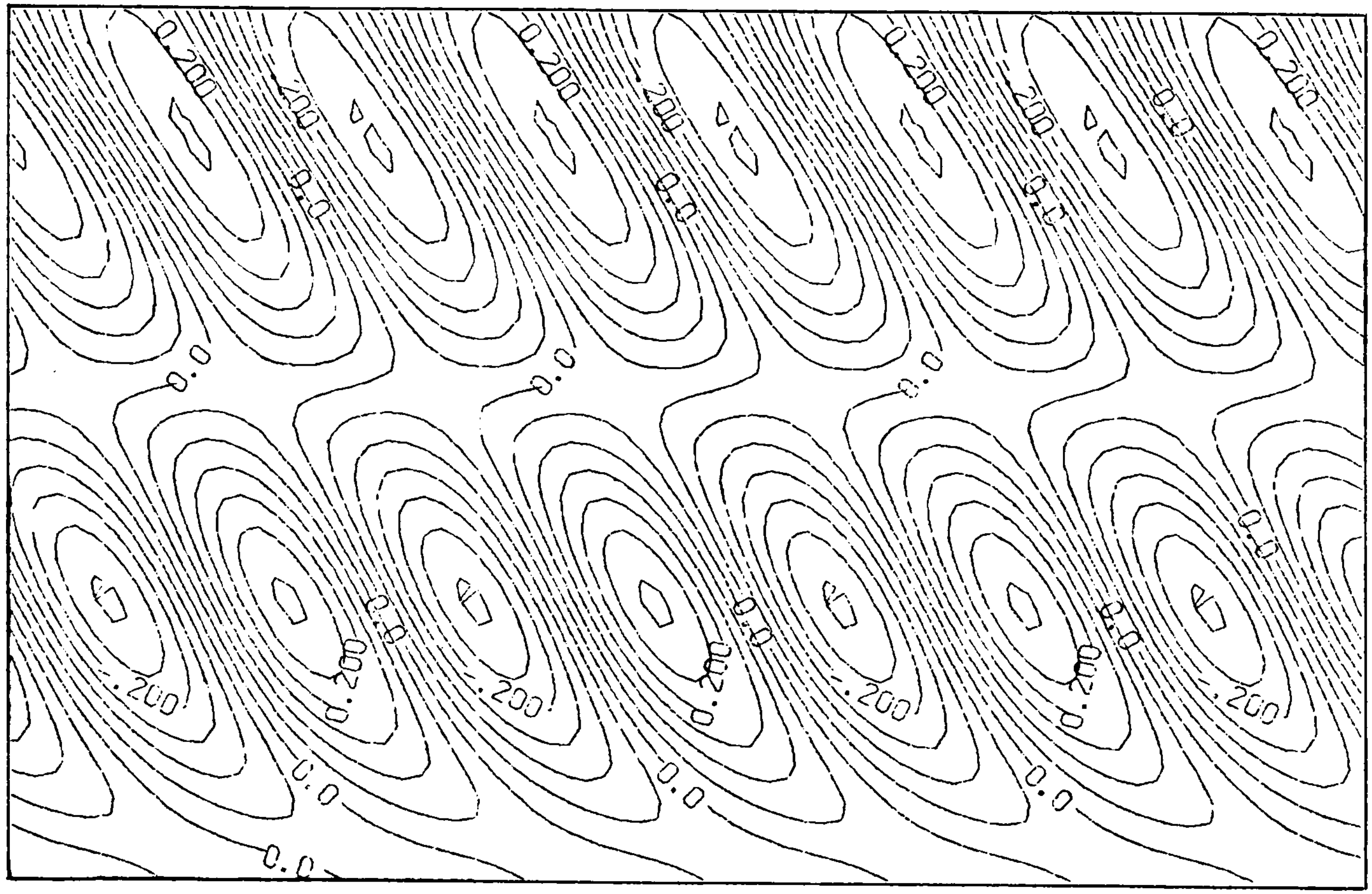

Figure 25. Contour of $\phi(x,y,1)$ at $t^* = 14$ Days.

low-pressure area. However, they are partitioned by dividing lines. They look like streamlines passing through an object because of steady waves (Figure 18) existing at this moment. At mid-height level, owing to the waves with very small amplitudes (Figure 19), only the curved dividing lines appear in Figure 24 without contours. At upper level, contours shown in Figure 25 have a number of oval shapes around low- (-0.200) or high- (0.200) pressure centers, and exhibit the atmospheric motion similar to cyclonic or anti-cyclonic motion. Each group of these concentric contours is separated from the other one by the curved dividing lines because the waves shown in Figure 20 have significant peaks and troughs. The wave cyclone develops in conjunction with a frontal zone. It is another possibility to make time integrations of A(k,l) and B(k,l) blow up finally because of frontogenesis.

Surface Plotting. The code SRFACE of the UTSI/NCAR package is used to draw a perspective picture of a function of two variables. The function is approximated by a two-dimensional array of heights. The lines of sight enter the horizontal plane from both the x and y directions at different angles.

The application of this code to the stream function $\phi(x,y,z)$ at different time produces the surfaces shown in Figures 26 through 29. The surfaces in Figures 26 and 28 were drawn with 41 grid points along the x and y directions, respectively, for clear appearance; while those in Figures 27 and 29 were drawn with 101 grid points along the x and y directions, respectively. Figure 26 indicates the surface of $\phi(x,y,1)$ which represents the very slight wavy surface at upper level and at initial time. This surface is nearly a flat one because

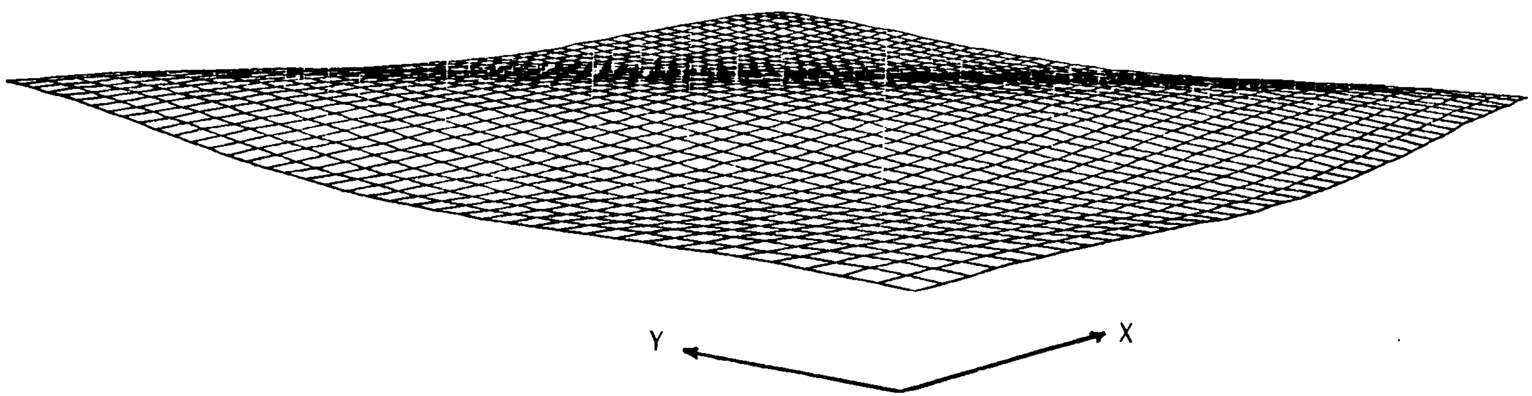

Figure 26. Surface of $\phi(x,y,1)$ at $t^* = 0$.

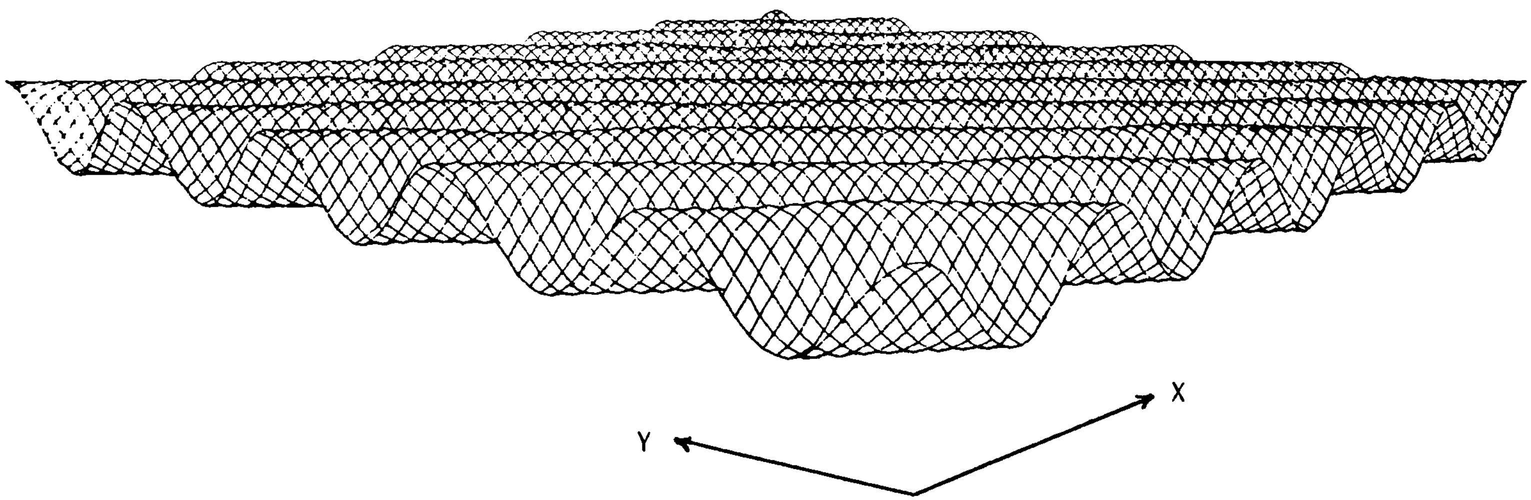

Figure 27. Surface of $\phi(x,y,0)$ at $t^* = 14$ Days.

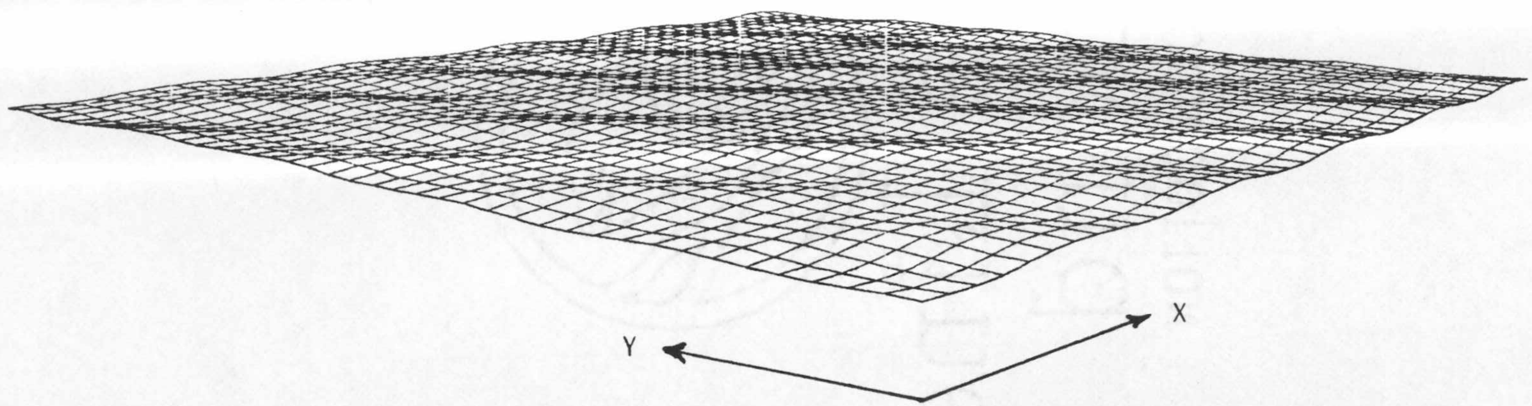

Figure 28. Surface of $\phi(x,y,\frac{1}{2})$ at $t^* = 14$ Days.

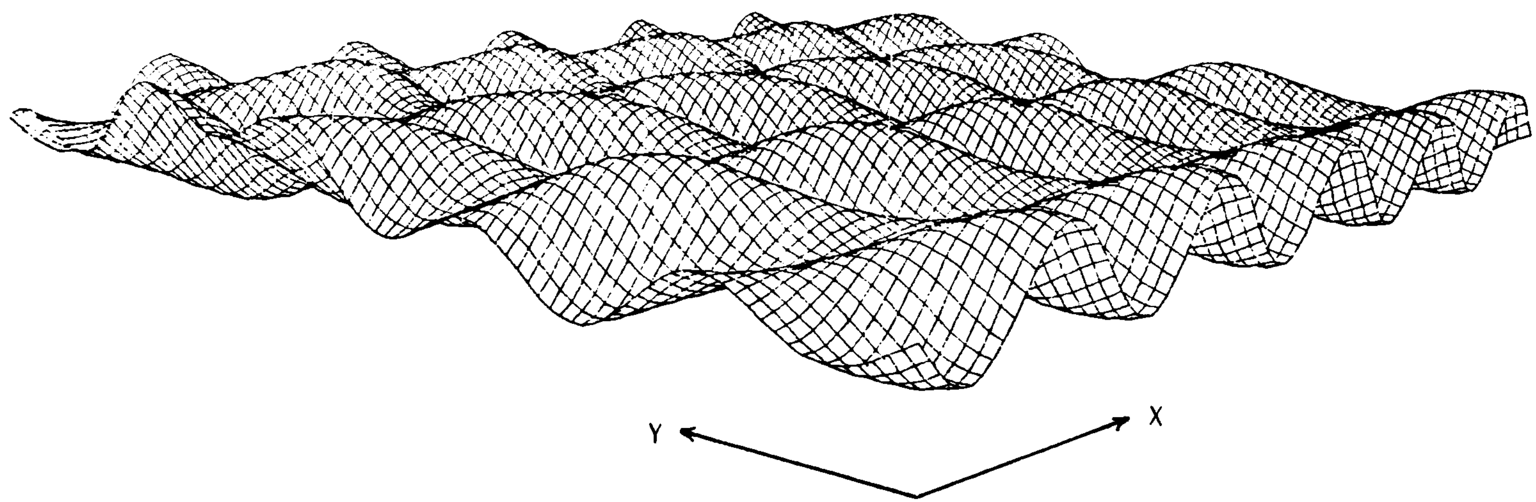

Figure 29. Surface of $\phi(x,y,1)$ at $t^* = 14$ Days.

the corresponding cosine wave in Figure 17 has the smaller wave amplitude. The other surfaces of $\phi(x,y,0)$ and $\phi(x,y,\frac{1}{2})$ at $t = 0$ are omitted because they are similar to the flat surface in Figure 26. At final time, 14 days, the surfaces obviously have the undulation, except for the surface in Figure 28 at mid-height level because the corresponding waves in Figure 19 have the very small amplitudes. The wavy surface in Figure 27 folds at wave peaks and troughs regularly owing to the nearly same amplitude waves in Figure 18. The surface in Figure 29 possesses a number of ups and downs on the surface. On both the x and y directions there are five wave ridges and five wave troughs coinciding with those shown in Figure 20.

Discussion of Waves, Contours, and Surfaces

The three-dimensional perturbation stream function $\phi(x,y,z,t)$ can be taken as a one-dimensional function at specific y, z, and t; and a two-dimensional function at specific height and time. These functions represent waves, contours, and surfaces shown in Figures 17 through 29. Comparing these figures, the following relationships are found: a) the waves predict what kind of contours or surfaces will produce, while the contours exhibit the surfaces rugged or not; and b) the surfaces justify the existence of waves and contours in different kinds and shapes. In this study, the figures for waves really predict the configurations of the surfaces, and the figures for contours exhibit these facts: a) closely spaced contours indicating the ruggedly wavy surface at upper level or uniformly wavy surface at lower level; and b) sparseness or absence of contours indicating the very weakly wavy surface or nearly flat x,y plane at mid-height level. These facts also indicate that the nonlinear instability in the baroclinic flow comes from the thermal wind shears because of the weak waves at mid-height level. From these facts, the strongly nonlinear theory and the structure of the code are proved to be applicable to the present study and the numerical computation, respectively.

CHAPTER VI

CONCLUSION

The development of our understanding of the complex nonlinear process occurring in baroclinic flows depends upon the interplay between theory, experiment, and field observation. Among these, three theory and numerical experiments were used in this investigation. The quasi-geostrophic potential vorticity equation leads to the nonlinear problem with boundary conditions, and this problem is solved numerically by the pseudospectral method.

A numerical computer code was written, developed, and verified to obtain the amplitudes A and B for the spectrally expanded solution which were found from the boundary conditions through time integration. The numerical experiments on the time integration for A and B indicate that a second-order Adams-Bashforth technique leads to superior results over the commonly used Runge-Kutta or the leapfrog methods. There are three factors which could make time evolution of A and B shorter or longer: 1) grid points, 2) physical plane size, and 3) initial values. The optimum results will depend on the combination of these three factors.

In the course of computation, the blow-up in time integration is a problem which puzzled us for a long time. The final time in integration was a few days, initially; however, we were able to stretch it to 14 days through many improvements. Though it is not the best one, it is really the better one in a lot of the numerical experiments. This perplexed problem comes possibly from the instability condition of the Eady linear model, atmospheric turbulence, and frontogenesis. Other reasons are not excluded here.

Examining the graphics for plane-wave presentation, contour and surface plottings, we find that at initial time the small amplitude cosine waves produce the tilted, parallel, straight lines (similar to isobars) or blank in contours, and the very slightly wavy surface. At ten days, the higher harmonic modes occur so late and so few that the plane wave and surface plottings are negligible, but two contours for $(x,y,\frac{1}{2})$ and $(x,y,1)$ are represented. From our numerical experiments, waves, contours, and surfaces at $t^* = 0$ and $t^* = 10$ days are similar to each other. However, at the final time, 14 days, wave patterns are different from one another at three vertical layers, i.e., at $z^* = 0$, 5 km, and 10 km heights. At the ground level, the wave would be steady wave, the contour lines look like streamlines passed through an object, and the surface is folded at wave peaks and troughs regularly. At the mid-height level, a train of waves has very small, different amplitudes. It makes the contour blank and the surface very slightly wavy. At the upper level another train of waves has substantially different amplitudes. It makes contours similar to cyclone (low-pressure center) followed by anti-cyclone (high-pressure center) and the wavy surface with ridges and troughs in both the x and y directions. Waves, contours, and surfaces exhibit that they exist consistently. The final wave surfaces at three different levels have the thermal wind-shear effect in the perturbed flow.

This investigation fails to predict the vacillation in a rotating annulus because the flow is inviscid and Ekman conditions are not introduced into it. The solution form in this study may lead to frontogenesis. If Ekman conditions are applied to both lower and upper boundaries, and if another solution form is used, it will be a different situation. This recommendation needs money and time for further study.

BIBLIOGRAPHY

BIBLIOGRAPHY

1. Charney, J. G. "The Dynamics of Long Waves in a Baroclinic Westerly Current," Journal of Meteorology. 4:135-163, 1947.

2. Eady, E. T. "Long Waves and Cyclone Waves," Tullus. 1:33-52, 1949.

3. Hide, R. and P. J. Mason. "Sloping Convection in a Rotating Fluid," Advances in Physics. 24:47-100, 1975.

4. Pedlosky, Joseph. "Finite Amplitude Baroclinic Waves," Journal of the Atmospheric Science, 27:15-30, 1970.

5. _____. "Finite Amplitude Baroclinic Waves with Small Dissipation," Journal of the Atmospheric Science, 28:587-597, 1971.

6. _____. "The Growth and Decay of Finite Amplitude Baroclinic Waves," Journal of the Atmospheric Science, 40:1863-1876, 1983.

7. Drazin, P. G. "Nonlinear Baroclinic Instability of a Continuous Zonal Flow," Quarterly Journal of the Royal Meteorological Society, 96:667-676, 1970.

8. _____. "Nonlinear Baroclinic Instability of a Continuous Zonal Flow of Viscous Fluid," Journal of Fluid Mechanics, 55:577-587, 1972.

9. Barcilon, A. and P. G. Drazin. "A Weakly Nonlinear Theory of Amplitude Vacillation and Baroclinic Waves," Journal of the Atmospheric Science, 41:3314-3330, 1984.

10. Chou, Shih-hung and Arthur Z. Loesch. "Supercritical Dynamics of Baroclinic Disturbances in a Free-Surface Model," Journal of the Atmospheric Science, 43:285-301, 1986.

11. _____. "Supercritical Dynamics of Baroclinic Disturbance in the Presence of Asymmetric Ekman Dissipation," Journal of the Atmospheric Science, 43:1781-1795, 1986.

12. Hoskins, B. J. "Baroclinic Waves and Frontogenesis Part I: Introduction and Eady Waves," Quarterly Journal of the Royal Meteorology Society, 102:103-122, 1976.

13. Boville, B. A. "Amplitude Vacillation on an f-Plane," Journal of the Atmospheric Science, 37:1413-1423, 1980.

14. _____. "Amplitude Vacillation of a β-Plane," Journal of the Atmospheric Science, 38:609-618, 1981.

15. ______. "Strongly Nonlinear Vacillation in Baroclinic Waves," Journal of the Atmospheric Science, 39:1227-1240, 1982.

16. Weng, Hengyi. "Strongly Nonlinear Dynamics of Baroclinic Waves," Ph.D. Dissertation, Florida State University, 1984.

17. Quinet, A. "A Numerical Study of Vacillation," Advances in Geophysics, 17:101-186, 1974.

18. Quon, Charles. "A Mixed Spectral and Finite Difference Model to Study Baroclinic Annulus Waves," Journal of Computational Physics, 20:442-479, 1976.

19. Williams, G. P. "Numerical Integration of the Three-Dimensional Navier-Stokes Equations for Incompressible Flow," Journal of Fluid Mechanics, 37:727-750, 1969.

20. Klein, Patrice and Joseph Pedlosky. "A Numerical Study of Baroclinic Instability at Large Supercriticality," Journal of the Atmospheric Science, 43:1243-1262, 1986.

21. Pedlosky, Joseph. Geophysical Fluid Dynamics. New York: Springer Verlag, 1979.

22. Panchev, S. Dynamic Meteorology. Holland: D. Reidel Publishing Company, 1985.

23. Lutgens, Frederick K. and Edward J. Tarbuck. The Atmosphere. New Jersey: Prentice-Hall, 1986.

24. Eliassen, Arnt and Kaare Pedersen. Meteorology, Vol. I, Physical Process and Motion. Oslo, Norway: Universitetsforlaget, 1977.

25. Hess, Seymour L. Introduction to Theoretical Meteorology. New York: Henry Hort and Company, 1959.

26. Gill, Adrian E. Atmosphere-Ocean Dynamics. New York: Academic Press, 1982.

27. Holton, James R. An Introduction to Dynamic Meteorology. New York: Academic Press, 1979.

28. Haltiner, G. J. Numerical Weather Prediction. New York: John Wiley and Sons, 1971.

29. Staniforth, Andrew N. and Roger W. Daley. "A Baroclinic Finite Element Model for Regional Forecasting with the Primitive Equations," Monthly Weather Review, 107:107-121, 1979.

30. Aksel, M. H, A. K. MacPherson and P. D. Hilton. "A Finite Element Study of Frontogenesis," Monthly Weather Review, 112:1053-1066, 1984.

31. Gottlieb, David and Steven A. Orszag. Numerical Analysis of Spectral Method: Theory and Applications. Philadelphia: Society for Industrial and Applied Mathematics, 1977.

32. Haltiner, G. J. and Roger T. Williams. Numerical Prediction and Dynamic Meteorology. New York: John Wiley and Sons, 1980.

33. Sela, Joseph G. "Spectral Modelling at the National Meteorological Center," Monthly Weather Review, 108:1279-1292, 1980.

34. Gottlieb, David, Liviu Lustman and Steven A. Orszag. "Spectral Calculations of One-dimensional Inviscid Compressible Flows," SIAM Journal on Scientific and Statistical Computing, 12:296-310, 1981.

35. Taylor, Thomas D., Robert B. Myers and Jeffrey H. Albert. "Pseudospectral Calculations of Shock Waves, Rarefaction Waves and Contact Surfaces," Computers and Fluids, 9:469-473, 1981.

36. Cornill, P. "A Pseudospectral Scheme for the Numerical Calculation of Shocks," Journal of Computational Physics, 47:146-159, 1982.

37. Hussaini, M. Y., D. A. Kopriva, M. D. Salas and T. A. Zang. "Spectral Methods for the Euler Equations: Part I--Fourier Methods and Shock Capturing," AIAA Journal, 23:64-70, 1985.

38. Voigt, Rober G., David Gottlieb and M. Yousuff Hussaini. Spectral Methods for Partial Differential Equations. Philadelphia: Society for Industrial and Applied Mathematics, 1984.

39. Burden, Richard L. and J. Douglas Fairs. Numerical Analysis. Boston: Prindle, Weberand, and Schmidt, 1985.

40. Roache, P. J. Computation Fluid Dynamics. Albuquerque, New Mexico: Hermosa Publishers, 1972.

41. Peyret, Roger and Thomas D. Taylor. Computational Methods for Fluid Flow. New York: Springer Verlag, 1983.

42. Weaver, H. Joseph. Applications of Discrete and Continous Fourier Analysis. New York: John Wiley and Sons, 1983.

43. Brigham, E. Oran. The Fast Fourier Transform. New Jersey: Prentice-Hall, 1974.

44. Elliot, Douglas F. and K. Ramamohan Rao. Fast Transforms. New York: Academic Press, 1982.

45. Cooley, J. W. and J. W. Tukey. "An Algorithm for the Machine Calculation of Complex Fourier Series," Mathematical Computations, 19:297-301, 1965.

46. Orszag, Steven A. "Spectral Methods for Problems in Complex Geometries, Journal of Computational Physics, 37:70-92, 1980.

VITA

Chieh Wu was born in Tungcheng County, Anhwei Province, China, on October 9, 1925. He was graduated from the National Fourth High School, and attended the National Central University where he received his Bachelor of Science degree in Aeronautical Engineering in 1948. After more than one year of training in the Chinese Air Force Technical School he was appointed instructor of the Chinese Air Force Academy in Taiwan, Republic of China, in 1950, and was promoted to Associate Professor there.

He began his graduate studies at the West Virginia University in September 1969, and received a Master of Science degree in Aerospace Engineering in August 1971. He then returned to Taiwan and served in the Aero-Industry Development Center for four years. As a Professor, he taught in the Chung Cheng Institute of Technology until he retired in December 1979.

In February 1980, he and his family immigrated to the United States at Oak Ridge, Tennessee. In the Winter Quarter of 1981 he entered The University of Tennessee Space Institute and continued his graduate research in Atmospheric Science. He received the degree of Doctor of Philosophy in Engineering Science in the Summer Quarter of 1987. He is a permanent member of the Aeronautical and Astronautical Society of the Republic of China. His book entitled <u>English and Chinese Dictionary of Aerospace Engineering Terms</u> was published in 1984.

Mr. Wu is married to the former Miss Hsiu-Fang Sun of Hopei Province, China. She graduated from the Law School of the National Taiwan University. They have two daughters: Ann, who received her Master of Science degree in Aerospace Engineering at The University of Illinois at Urbana and Champaign in 1983; and Alice, a graduate student in the Electrical Engineering Department of The University of Tennessee, Knoxville, in 1987.